Simulation and Evaluation of Non-Injection,Voltage Sensing-Based Flux Tracking Self-Sensing for SPMSMs for Zero-to-Low Speeds

by

Carlos Martínez Diez

Submitted to the Department of Electrical Engineering, Electronics, Computers and Systems
in partial fulfillment of the requirements for the degree of
Master Course in Electrical Energy Conversion and Power Systems
at the
UNIVERSIDAD DE OVIEDO
July 2014

Author……
Carlos Martínez Diez
Master Student
Certified by……
Pablo García Fernández
Full Professor
Thesis Supervisor
Certified by……
Robert D. Lorenz
Research Fellow
Thesis Supervisor

Simulation and Evaluation of Non-Injection,Voltage Sensing-Based Flux Tracking Self-Sensing for SPMSMs for Zero-to-Low Speeds

by

Carlos Martínez Diez

Submitted to the Department of Electrical Engineering, Electronics, Computers and Systems

on July 23, 2014 in partial fulfillment of the

requirements for the degree of

Master Course in Electrical Energy Conversion and Power Systems

Abstract

The goal of this project is to develop and evaluate a simulation model of a self-sensing method based on flux tracking using measured phase voltage for motion control in the zero-to-low speed operation range of surface permanent magnet synchronous machines (SPMSMs). The limitation of previous non-injection based self-sensing methods, especially at zero-to-low speed, is an inaccurate voltage reference due to inverter nonlinearities and a back-EMF term which approaches zero frequency as speed does. This research focuses on a thorough investigation of the limitations of back-EMF tracking at zero-to-low speeds with measured phase voltages, using a patented, but relatively undocumented methodology to measure back-EMF at zero-to-low speeds. The induced voltage and current responses to the permanent magnet flux at zero-to-low speeds is modeled and simulated under a variety of conditions in order to determine the optimal position state filter or observer. The resultant motion control system is evaluated via dynamic stiffness and under a set of different conditions of torque load (T_L) in order to determinate the limitations of this flux tracking approach. The outcome of this research is an understanding of the effects of bandwidth selection for the PLL and

motion and current controllers, an evaluation of the disturbance rejection capabilities of closed loop control at zero-to-low speeds, and a method for using measured stator voltage for enhanced zero-to-low speed position estimation for flux tracking self-sensing methods.

Thesis Supervisor: Pablo García Fernández
Title: Full Professor

Thesis Supervisor: Robert D. Lorenz
Title: Research Fellow

Acknowledgments

.

Contents

List of Figures

List of Tables

Chapter 1

Introduction

1.1 Project Overview

One of the most popular methods of self-sensing (sensorless) control consists of tracking the back-electromotive force (back-EMF) of Permanent Magnet Synchronous Machines (PMSMs). The problem with this approach is that it fails when working at zero-to-low speeds, since the back-EMF amplitude and frequency are both proportional to the rotor speed. This occurs due to the fact that the back-EMF is generally estimated from the available signals in the inverter which contain inverter harmonics, and as a result, the lower the speed the lower the signal-to-noise ratio. In addition, at zero speed, the only signal measured is the inverter harmonics. Therefore, at low speeds, the speed signal from the back-EMF tracking estimator is typically filtered which reduces the dynamic stiffness of the system in proportion to the speed. This is why at zero-to-low speeds high frequency injection methods are commonly used rather than back-EMF tracking.

This research analyzes the method for low speeds proposed and implemented by Dr. Andre Veltman in his patent “Method and a Device for Sensorless Estimating the Relative Angular Position between the Stator and the Rotor of a Three-Phase

Synchronous Motor" [27]. The reason for doing that is to know the validity and limitations of this method as it has not been discussed in other literature.

1.2 Research Contributions

The research contributions are related to the discussion about the validity of the proposed method by Veltman and understand the limitations of his approach. Furthermore, it will be discussed whether there is room for improvement in this field and if so, where the further research should be focused on.

1.3 Overview of Chapters

Chapter 1 reviews the state-of-the-art in regard to self-sensing methods to estimate rotor position at zero-to-low speeds. In addition to that, the modelling of a PMSM is explained too. Among the commonly used self-sensing methods there are high-frequency injection techniques and back-EMF tracking techniques. With regard to the high-frequency injection techniques, rotating and pulsating voltage injection methods are considered; as well as some implementation issues concerning these HF injection methods. With regard to back-EMF tracking, the literature and previous work involving flux linkage estimation, extended Kalman filters and observers is reviewed. Finally, the Veltman's patent is reviewed to understand the methodology that he patented.

Chapter 2 describes the implementation and evaluation of the flux tracking self-sensing method shown in his patent in *Simulink* and the simulation work is split up in

different sections. This chapter documents the simulation work carried out and shows the simulation results that Veltman claimed to achieve in his patent. Different aspects of the simulation implementation are covered in detail such as the controllers tuning, the arctangent implementation and the Phase-Locked-Loop (PLL) used to get the position and velocity estimates. Implementation issues in that regard are also addressed in this section.

Chapter 3 evaluates the simulation results concerning position and velocity estimation. Also the current ratings with different load torques are analyzed. Furthermore, a further evaluation of the simulation model via the dynamic stiffness and the parameter sensitivity analysis.

Chapter 4 addresses the conclusions obtained from the research, summarizes the contributions of the work and gives some recommendations for future work.

Chapter 2

Review of the Start of the Art

This chapter reviews the state-of-the-art related to self-sensing methods for zero-to-low speeds in SPMSMs. The first part of the chapter explains the different designs of PMSMs and how the machines are modelled. Secondly, the high frequency injection methods that are commonly used for back-EMF tracking at zero-to-low speeds for the SPMSMs are discussed.

This type of machines have some desirable features like the high efficiency and low torque ripple that make them suitable for a wide range of applications like high torque and low speed motion control. In addition to that, they are cost-effective. One important characteristic of SPM machines is their symmetric rotor structures. It results in low spatial inductance variation and typically makes SPM machines have nearly zero saliency features. Under this effect, self-sensing closed-loop control might be limited at only no loaded condition. For SPM machines, self-sensing closed-loop control is still a challenge, and usually must compromise by using a low-resolution position sensor or open-loop control at zero and low speeds.

This research starts from the-state-of-art review of both high performance PM machine design and self-sensing estimation methodologies. Firstly, the modelling of a PM machine is described and afterwards the different self-sensing techniques are discussed.

2.1 PMSM Modelling

In regard to the machine rotor design PMSMs are divided into two categories which are IPMSMs and SPMSMs as Fig. 2.1 shows.

The first kind has the magnets buried in the rotor whereas the second one has them placed on the surface of the rotor. Having the magnets embedded in the rotor makes the IPMSM able to produce some reluctance torque, as the inductances in the d and q axis are not equal, in addition to the magnetic torque produced by the PM; on the other hand, the symmetry of the rotor configuration in SPMSMs allows this machines to produce a low torque ripple which it is required in direct-drive applications. [1-3]. One drawback of the SPMSMs topology is the lower mechanical robustness as the PMs are not actually fitted into the rotor laminations like the IPMSMs, and this does not allow the machine to operate at very high speeds due to high centrifugal forces on the magnets.

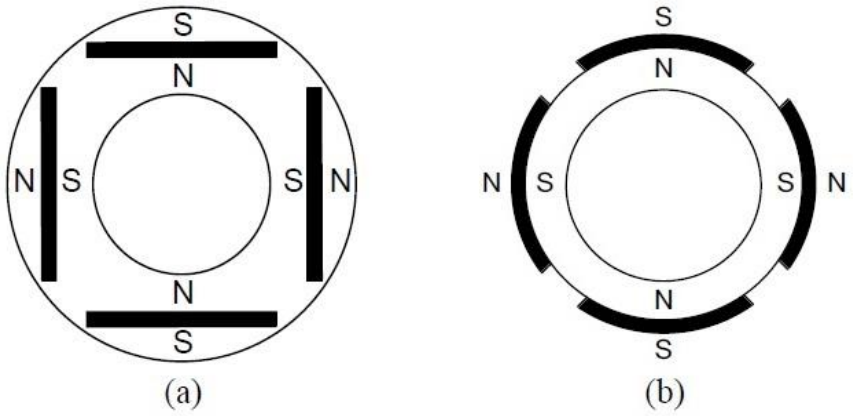

Fig. 2.1- Rotor configurations for an IPMSM (a) and a SPMSM (b) [3]

The machine equations of a PMSM are usually shown in a d-q synchronous reference frame. In order to express the abc stationary reference frame machine equations in an arbitrary dq reference frame the following transformation matrix K must be used as shown in (1-1) [4,5].

$$f_{dq0} = K\, f_{abc} = \frac{2}{3}\begin{bmatrix} \cos\theta & \cos\left(\theta - \frac{2\pi}{3}\right) & \cos\left(\theta + \frac{2\pi}{3}\right) \\ \sin\theta & \sin\left(\theta - \frac{2\pi}{3}\right) & \sin\left(\theta + \frac{2\pi}{3}\right) \end{bmatrix} f_{abc} \qquad (2\text{-}1)$$

The general voltage equations for a PMSM are shown for both d and q axis in the synchronous (rotor) reference frame (1-2) and (1-3). In the particular case of a SPMSM 'L_d' and 'L_q' are of the same value.

$$V_{ds}^{r} = R_s\, I_{ds}^{r} + p\lambda_{ds}^{r} - \omega_r\, \lambda_{qs}^{r} \qquad (2\text{-}2)$$

$$V_{qs}^{r} = R_s\, I_{qs}^{r} + p\lambda_{qs}^{r} - \omega_r\, \lambda_{ds}^{r} \qquad (2\text{-}3)$$

Being

$$\lambda_{ds}^{r} = L_d\, I_{ds}^{r} + \lambda_{PM} \qquad (2\text{-}4)$$

$$\lambda_{qs}^{r}=L_q I_{qs}^{r} \tag{2-5}$$

If we substitute the flux linkage terms in (1-4) and (1-5) into (1-2) and (1-3) it is obtained the following voltage equations in the rotor reference frame.

$$V_{ds}^{r}=R_s I_{ds}^{r} + L_d \frac{d}{dt} I_{ds}^{r} - \omega_r L_q I_{qs}^{r} \tag{2-6}$$

$$V_{qs}^{r}=R_s I_{qs}^{r} + L_q \frac{d}{dt} I_{qs}^{r} + \omega_r (L_d I_{ds}^{r}+\lambda_{PM}) \tag{2-7}$$

(1-8) shows the electromagnetic torque equation of a PMSM, 'P' being the number of poles of the machine. From the torque equation it may be appreciated that there is a term proportional to the q-axis current and the PM flux linkage and another term (reluctance torque) which appears when the machine has some saliency (L_q>L_d). The latter is the case of the IPMSMs.

$$T_{em}=\frac{3}{4}P\left[\lambda_{PM} I_{qs}^{r} - (L_d - L_q) I_{qs}^{r} I_{ds}^{r}\right] \tag{2-8}$$

2.2 High-Frequency Injection Methods

At low speeds or standstill, the magnetic saliency of the machine can be used to estimate the rotor position. This is what is done in high-frequency injection methods. In theory SPMSMs have no saliency as the inductances in the d and q axis are nearly equal. However, there are some saliencies caused by the magnetic saturation of the stator due to the PM flux.

The working principle of these techniques is that a high-frequency current or voltage signal is superimposed to the fundamental excitation of the machine and the resultant current will be analyzed to determine both the flux and rotor position. The magnetic axis location is usually estimated by using the carrier signal current whilst the location of the

magnet is tracked by using saliency image. The saliency image represents the special inductance distribution along the rotor and varies with the operating conditions with respect to the fundamental excitation [2].

2.2.1 Rotating Carrier Frequency Voltage Injection

This method basically consists of injecting a rotating voltage signal in the stationary reference frame and trying to analyze the corresponding current response signal to extract the position information throughout a demodulation process [6].

(1-9) shows the high frequency model in a complex vector form in the stationary reference frame of an IPMSM which has a magnetic saliency of an 'h' order harmonic.

$$V_{dqs}^{s}=R_s I_{dqs}^{s} + \left(p\Sigma L I_{dqs}^{s} - \Delta L e^{jh\theta_e} I_{dqs}^{s}\right) + \omega_r \lambda_{PM} e^{j\theta_r} \quad (2\text{-}9)$$

Where $\Sigma L=\frac{L_d + L_q}{2}$ and $\Delta L=\frac{L_d - L_q}{2}$.

If the previously mentioned high frequency vector is injected (1-10) into the IPMSM, a high frequency current is produced (1-11) neglecting the resistance drop and the back-EMF term of the equation.

$$V_{dqs}^{s}=V_c e^{j\theta_c} \quad (2\text{-}10)$$

$$I_{dqs}^{s}= -jI_{cp} e^{j\omega_c} - jI_{cn} e^{j(-\omega_c \pm h\theta_e)} \quad (2\text{-}11)$$

Where $\omega_c=\frac{d\theta_c}{dt}$

As stated in [7], the second term of (1-11) contains the position information. In this paper the following demodulation scheme (Fig. 2.2) is proposed, in which the negative sequence component of current signal is extracted throughout filters and rotation of the

reference frame. Alternatively, in [6] a different demodulation process is proposed (heterodyining). In this paper the high frequency component is extracted from the measured current signal through a band-pass-filter and taken into the aforementioned heterodyining process (Fig. 2.3) in which the high frequency components are multiplied by a sinusoidal function of the same injection frequency and will be filtered by a low pass filter to get the final error signal 'εf' that would input the state filter.

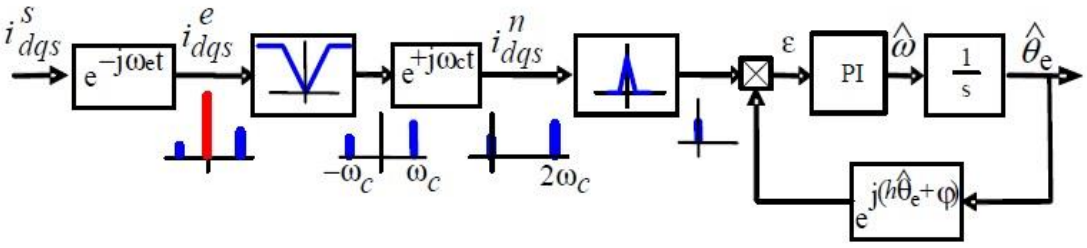

Fig. 2.2- Rotating voltage vector injection-based position tracking state filter. [7]

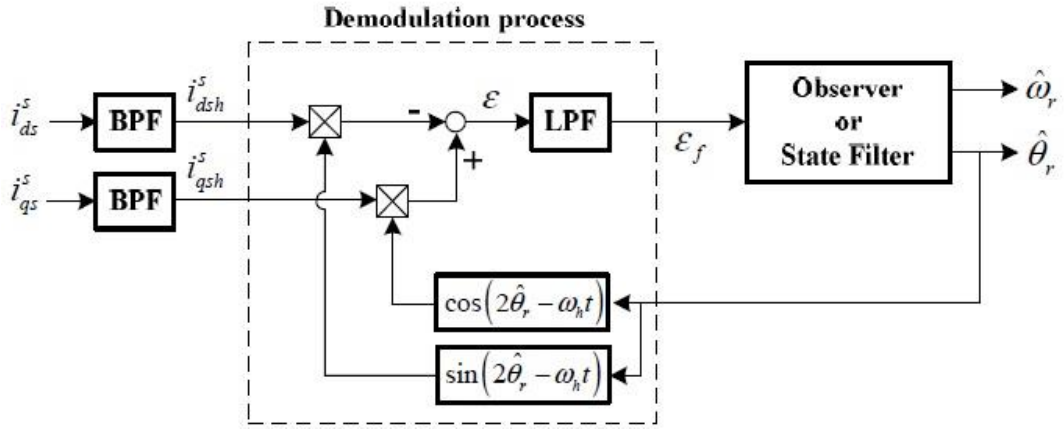

Fig. 2.3- Demodulation process in rotating voltage injection method [6]

2.2.2 Pulsating Carrier Frequency Voltage Injection in the Estimated d-axis

In this method, a high frequency voltage signal (1-12) is injected in the estimated d-axis synchronous frame of the IPMSM. The resulting stator flux is obtained by

integrating the carrier voltage signal (1-13) and neglecting the voltage drop in the stator resistance and the back-EMF term as it has been done in (1-9).

$$\hat{V}^{r}_{ds}=V_c \cos \omega_c t \tag{2-12}$$

$$\lambda^{r}_{dqsc} \approx V^{r}_{dqsc}\, dt = \frac{V_c}{\omega_c} \sin \omega_c t \,(\cos\theta_{err} - j\sin\theta_{err}) \tag{2-13}$$

Where $\theta_{err} = \theta_r - \hat{\theta}_r$

The high frequency current components that contain the position information result from the interaction of the carrier voltage and the saliencies as explained in [6]. The current expression can be simplified to (1-14):

$$\hat{I}^{r}_{dqsc} = \left(I_{cdc} + I_{c2\theta_{err}}\, e^{j2\theta_{err}}\right) \sin \omega_c \tag{2-14}$$

Fig. 2.4 shows the rotor flux and the injected voltage in the dq reference frame and in the estimated dq reference frame respectively when it is not estimated correctly. Additionally, (1-14) can be split up into the d-axis and q-axis components (1-15) (1-16) as it is done in [8]. This way, by controlling the q-axis current component to be zero position error may be regulated to be zero as well.

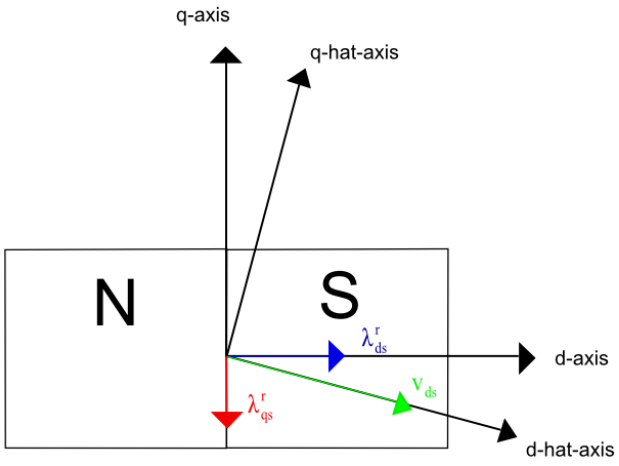

Fig. 2.4- Rotor flux in the dq reference frame and injected voltage in the estimated dq reference frame

$$\hat{I}^{r}_{dsc} = I_{cdc} \sin \omega_c t + I_{c2\theta_{err}} \cos 2\theta_{err} \sin \omega_c t \quad (2\text{-}15)$$

$$\hat{I}^{r}_{qsc} = I_{c2\theta_{err}} \sin 2\theta_{err} \sin \omega_c t \quad (2\text{-}16)$$

2.2.3 Implementation Issues with HF Injection Methods

It is noteworthy to point out that there are some issues when implementing HF injection techniques. In [9] some implementation issues are discussed, such as the non-linear behavior of pulse-width modulation and power electronics, the signal processing and variations in the saliency.

Usually, for motor drives applications a three-phase PWM inverter is used, which introduces non-linearities into the system. These non-linearities affect highly to the carrier signal due to its low magnitude and high frequency. The performance of the self-sensing control is therefore compromised when distortion or harmonics are present in the carrier signal. The effects of the inverter harmonics are shown in Fig. 2.5 when using a PWM inverter in a) and c) and a linear inverter in b). Moreover, an anti-aliasing filter

was used in c). By looking at the figure it is clearly seen that only in the first case (PWM inverter and without low-pass filter) harmonics are present at $\pm\omega_e$, which means that must be caused by the inverter switching and aliasing as they are easily removed by a low-pass filter.

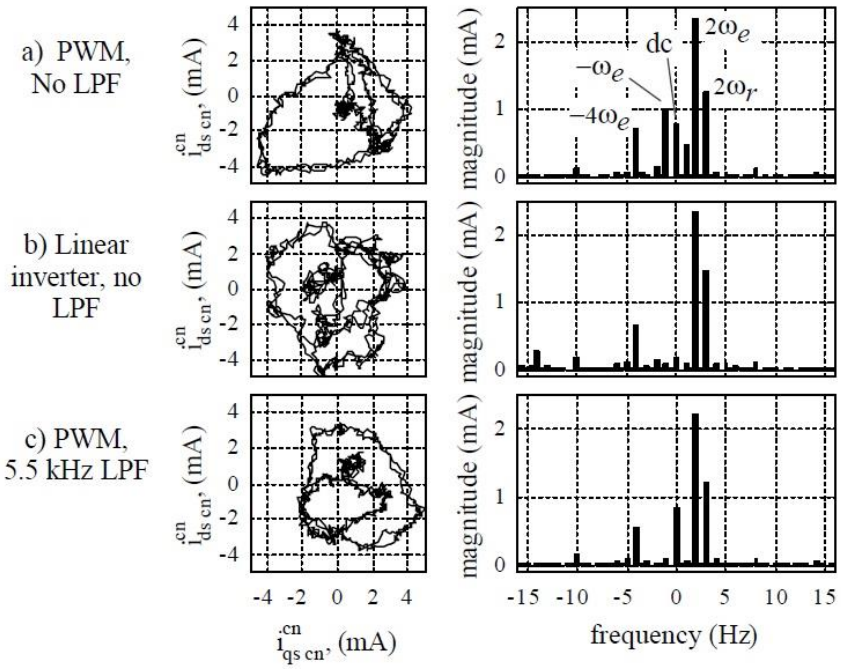

Fig. 2.5- Negative sequence carrier signal current trajectory and spectrum in the negative sequence carrier signal reference frame under open-loop operation [9].

Further in [9] the effect of the dead time in the inverter is analyzed as well. Furthermore, the selection of both the magnitude and frequency of the carrier signal is restricted to some concerns. The upper limit for the frequency selection is given by the Nyquist criterion and also by the signal-to-noise ratio which decreases as the carrier frequency increases. As for the lower limit for the carrier frequency, it must be ensured

that there is enough spectral separation from the fundamental frequency so that the necessary filtering stage may be implemented.

In regards to the carrier signal magnitude selection, the lower limit is given by the non-linearities of the inverter and the current feedback. The upper limit must be set taking into consideration the required power and the audible noise that will be introduced.

In [9] two different carrier frequencies (250 and 3750Hz) have been considered, for the latter case (3750Hz) harmonics at $\pm\omega_e$ appear, caused by the inverter and aliasing. Also, as the carrier frequency increases, the $\pm\omega_e$ harmonics magnitude increases as well. Therefore it can be concluded that the magnitude and spatial position of these harmonics is closely related to the stator current, being easy to decouple. However, at high carrier signal frequencies, they may have a great impact on the estimation accuracy because of their big magnitude.

Some temperature issues are addressed in [10]. Considering three different carrier signal excitation methods (rotating voltage injection, pulsating voltage injection and square-wave carrier voltage injection). The experimental results are shown in Fig. 2.6, where the different stator temperatures are measured for the different excitation methods.

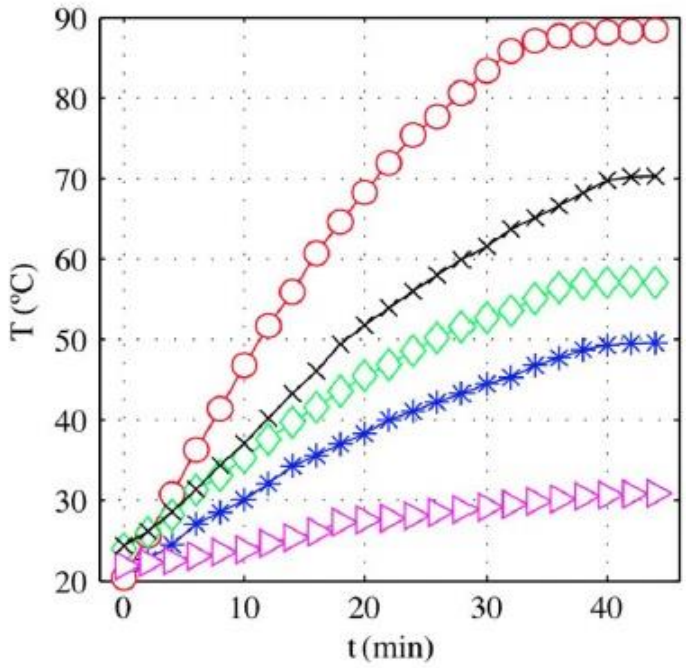

Fig. 2.6- Measured stator temperatures. Rotating carrier signal excitation: (o) 2500 Hz and (∗) 500 Hz. Pulsating carrier signal excitation: (♦) 2500 Hz and (►) 500 Hz. Square-wave carrier signal excitation: (x) 5000 Hz [10].

The first conclusion that may be extracted from Fig. 2.6 is that higher carrier signal frequencies produce larger temperature increases. It is also observed that for the same magnitude of carrier signal current, pulsating carrier signal excitation shows lower losses than the other carrier signal excitation methods. This way, the selection of the excitation frequency ends up being a tradeoff between temperature increase and self-sensing performance, since higher frequencies are beneficial in regards to the self-sensing control. This paper also states that the IPMSMs are desired in terms of machine losses over the SPMSMs for their use with saliency-tracking-based self-sensing methods.

2.3 Back-EMF Tracking

Back-EMF tracking is another self-sensing method to estimate the rotor position. As it has already been mentioned before, the back-EMF is proportional to the rotor speed and therefore it becomes challenging to track at low speeds. The low speed limits are discussed in [11] where it is concluded that the limits are fully dependent on the amount of noise introduced by inverter harmonics on the estimated speed signal. As presented in [4] there are different subcategories when it comes to back-EMF tracking which are the flux linkage estimation, the extended Kalman filter (EKF) and the observer-based methods.

2.3.1 Flux Linkage Estimation

This chapter reviews the state-of-the-art related to self-sensing methods for zero-to-low speeds in SPMSMs. The first part of the chapter explains the different designs of PMSMs and how the machines are modelled. Secondly, the high frequency injection methods that are commonly used for back-EMF tracking at zero-to-low speeds for the SPMSMs are discussed.

The PM rotor flux position can be obtained by integrating the measured back-EMF [11, 12, 13]. The accuracy of this method strongly depends on the estimation of the machine parameters such as the stator resistance 'R_s' and the inductances 'L_d' and 'L_q'.

Considering the voltage equations of the PMSM in the stationary reference frame (1-17), (1-18), they may be rewritten to solve for the flux linkage (1-19), (1-20).

$$V_{ds}^{s} = R_s I_{ds}^{s} + p\lambda_{ds}^{s} \quad (2\text{-}17)$$

$$V_{qs}^{s} = R_s I_{qs}^{s} + p\lambda_{qs}^{s} \quad (2\text{-}18)$$

$$\lambda_{ds}^{s} = \int V_{ds}^{s} - R_s I_{ds}^{s} \quad (2\text{-}19)$$

$$\lambda_{qs}^{s} = \int V_{qs}^{s} - R_s I_{qs}^{s} \quad (2\text{-}20)$$

For the case of the SPMSM, the rotor flux linkages can be obtained from the stator ones as shown in (1-21), (1-22). Finally, the angle of the rotor flux linkages which ultimately allows determining the rotor position is calculated by using the arctangent (1-23).

$$\lambda_{dr}^{s} = \lambda_{ds}^{s} - L_s I_{ds}^{s} \quad (2\text{-}21)$$

$$\lambda_{qr}^{s} = \lambda_{qs}^{s} - L_s I_{qs}^{s} \quad (2\text{-}22)$$

$$\angle \lambda_{dqr}^{s} = \arctan\left(\frac{\lambda_{qr}^{s}}{\lambda_{qr}^{s}}\right) \quad (2\text{-}23)$$

This direct calculation method to estimate position will produce a noisy estimate as the measured signals always contain some noise. The arctangent will actually amplify the noise due to the fact that if 'L_d' and 'L_q' are small a small change in them will create a big change in the angle between them. The noise might be filtered out by using a filter but this will add a lag to the estimate which is not desired.

2.3.2 Extended Kalman Filter

The Extended Kalman Filter (EKF) is a mathematical model used to estimate unmeasured states. It varies the gains to filter out the noise of the estimated variables [4, 14].

Unlike other back-EMF approaches, the EKF does not require knowledge of the mechanical parameters of the motor. The algorithm it uses, updates constantly the value of the gain 'K' to reject the noise. As the 'K' value varies with the noise, so does the bandwidth of the EKF, which means that the more noise the system has, the lower the bandwidth is.

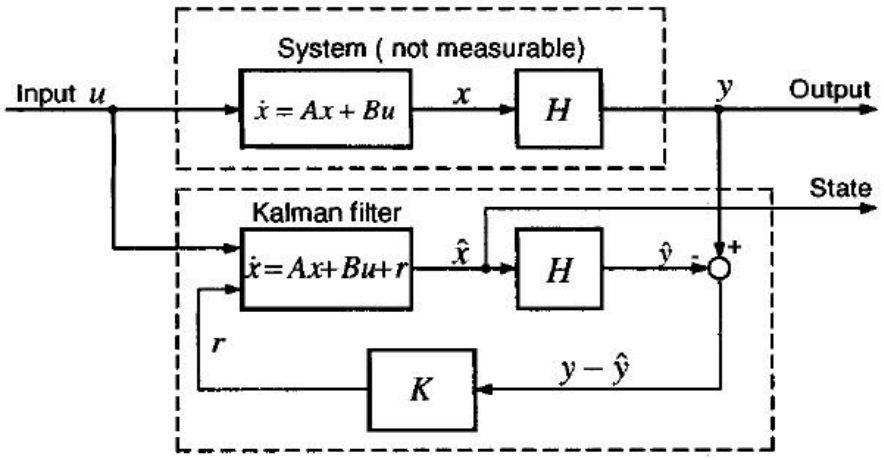

Fig. 2.7- EKF Scheme [15]

(1-24) and (1-25) are the non-linear state equations of a PMSM that must be considered to apply the EKF [4, 15, 16, 17, 18].

$$\dot{x} = f\,[x(t)] + B \cdot v(t) + \sigma(t) \qquad (2\text{-}24)$$

$$y(t_k) = h(x(t_k)) + \mu(t_k) \qquad (2\text{-}25)$$

Where 'x' and 'y' are the input and output states variables respectively, '$\sigma(t)$' is the system noise and '$\mu(t_k)$' the measured one. Both noise variables have a zero-mean white Gaussian distribution. In addition, '$Q(t)$' and '$R(t_k)$' are respectively the covariance of '$\sigma(t)$' and '$\mu(t_k)$'.

Considering the machine equations in the stationary (αβ) reference frame for a SPMSM and that $x = [I_\alpha\ I_\beta\ \omega\ \theta]$, $y = [I_\alpha\ I_\beta]$ and $v = [v_\alpha\ v_\beta]$ the system matrices might be written as it follows [15,16]:

$$f[x] = \begin{bmatrix} f_1 \\ f_2 \\ f_3 \\ f_4 \end{bmatrix} = \begin{bmatrix} \frac{-R_s I_\alpha + \omega\lambda_{PM}}{L_s} \sin\theta \\ \frac{-R_s I_\beta - \omega\lambda_{PM}}{L_s} \cos\theta \\ 0 \\ \omega \end{bmatrix}, \quad B = \begin{bmatrix} \frac{1}{L_s} & 0 \\ 0 & \frac{1}{L_s} \\ 0 & 0 \\ 0 & 0 \end{bmatrix}, \quad h[x] = \begin{bmatrix} I_\alpha \\ I_\beta \end{bmatrix}$$

A method to tune the covariance matrices is explained in [19], in which the EKF algorithm is normalized so it may work for different drivers.

The limitations of the EKF are discussed in [20] and it is concluded that the EKF may not converge if the operating point is far from the true state. Moreover, some assumptions are made like the Gaussian representation of the uncertainties which might be inaccurate.

Some simulation and experimental results are shown in [21] for a SPMSM using the EKF to estimate both position and velocity (Fig. 2.8). It may be appreciated that the Kalman filter can estimate the exact rotor speed and rotor position while the initial position and mechanic parameters are not needed. However, the covariance matrixes of noises can only be determined by experimentally since the noises and disturbances are not known in practice.

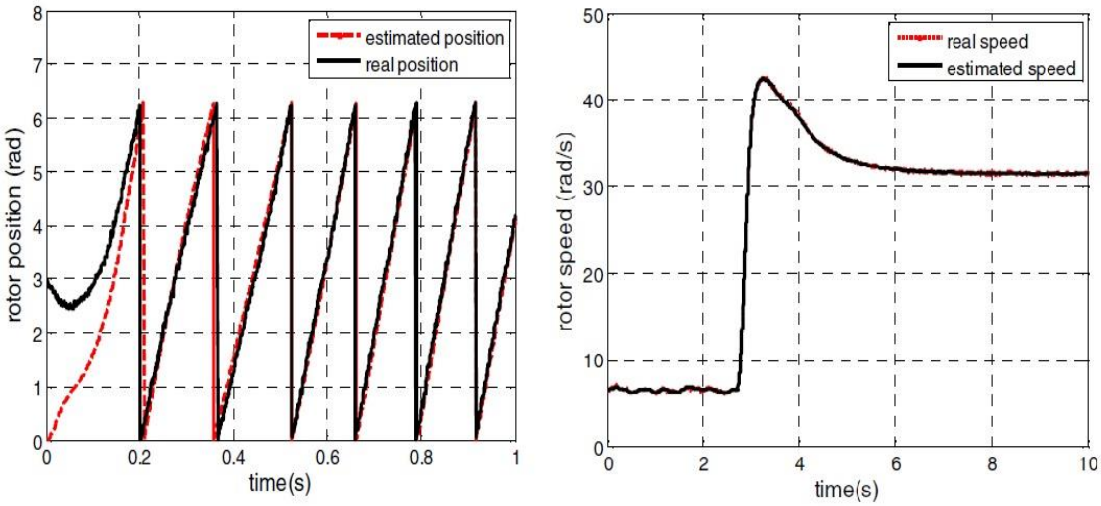

Fig. 2.8- Position estimate (left) and velocity estimate (right) using EKF [22]

2.3.3 Observer

An observer is a mathematical model of a physical system that runs parallel to it and takes as inputs measured states from the physical model to estimate other states. The back-EMF induced in the motor is an electrical variable for which, with the measured current, a closed-loop position control may be implemented. Furthermore, the back-EMF contains in itself the rotor position information and therefore the position can be estimated directly. Kim [2][22] developed a state filter to estimate the saliency-based EMF in the stationary reference frame in cascade with tracking observer to estimate the position; later, Hejny [4] implemented a back-EMF state filter and the enhanced Luenberger style back-EMF observer in his Master Thesis.

In [22] saliency-based EMF methods are described, these methods are mainly intended for an IPMSM in which there is some saliency. (1-26) shows the voltage equations of an IPMSM in the rotor reference frame whereas (1-27) shows the saliency-

based EMF term in the rotor reference frame. This latter term may be also expressed as a rotating vector in the stationary reference frame (1-28).

$$\begin{bmatrix} V_{ds}^{s} \\ V_{qs}^{s} \end{bmatrix} = \begin{bmatrix} R_s + pL_d & -\omega_r L_q \\ \omega_r L_q & R_s + pL_d \end{bmatrix} \begin{bmatrix} I_{ds}^{s} \\ I_{qs}^{s} \end{bmatrix} + \begin{bmatrix} 0 \\ E_{sal} \end{bmatrix} \tag{2-26}$$

$$E_{sal} = \omega_r \left| (L_d - L_q) I_{ds}^{r} + \lambda_{PM} \right| - (L_d - L_q) p I_{qs}^{r} \tag{2-27}$$

$$\begin{bmatrix} E_{sal\_ds}^{s} \\ E_{sal\_qs}^{s} \end{bmatrix} = E_{sal}^{s} \begin{bmatrix} -\sin\theta_r \\ \cos\theta_r \end{bmatrix} \tag{2-28}$$

The position can be estimated using different methods, but in this section only the observer-based ones will be discussed (state-filter and observer). The state filter and the observer topologies are very similar to each other; nevertheless the observer topology includes a feedforward term which makes the estimate to have almost zero lag whereas the state filter has inherently lagging properties. Some of the advantages that observers have over the arctangent method are the larger signal-to-noise ratio and the possibility to track multiple saliencies [23].

The first observer-based estimation method proposed in [22] is a state filter to track the saliency-based EMF (Fig. 2.9) consisting in the IPMSM model with a PI regulator which will estimate the saliency-based EMF within the state filter bandwidth. At high speeds, the timing delays in the controller and in the inverter caused by the use of commanded voltages as feedforward and measured currents as the state reference must be included in the model.

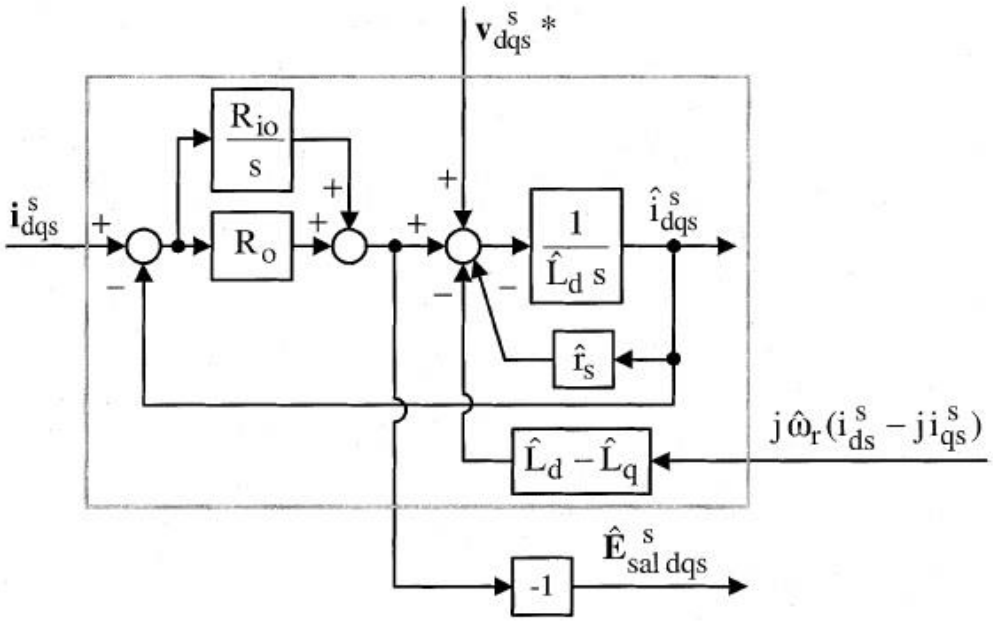

Fig. 2.9- Saliency-based EMF state filter [22]

The second observer-based estimation method proposed in [22] is the enhanced Luenberger style back-EMF tracking observer (Fig. 2.10). The estimated saliency term from the state filter containing the rotor position information (1-29) is the input of the observer. A cross-product (1-30) has been used to produce the error signal that inputs the regulator. The electromagnetic torque command is added as a feedforward term to the output of the PI regulator to achieve zero-phase lag.

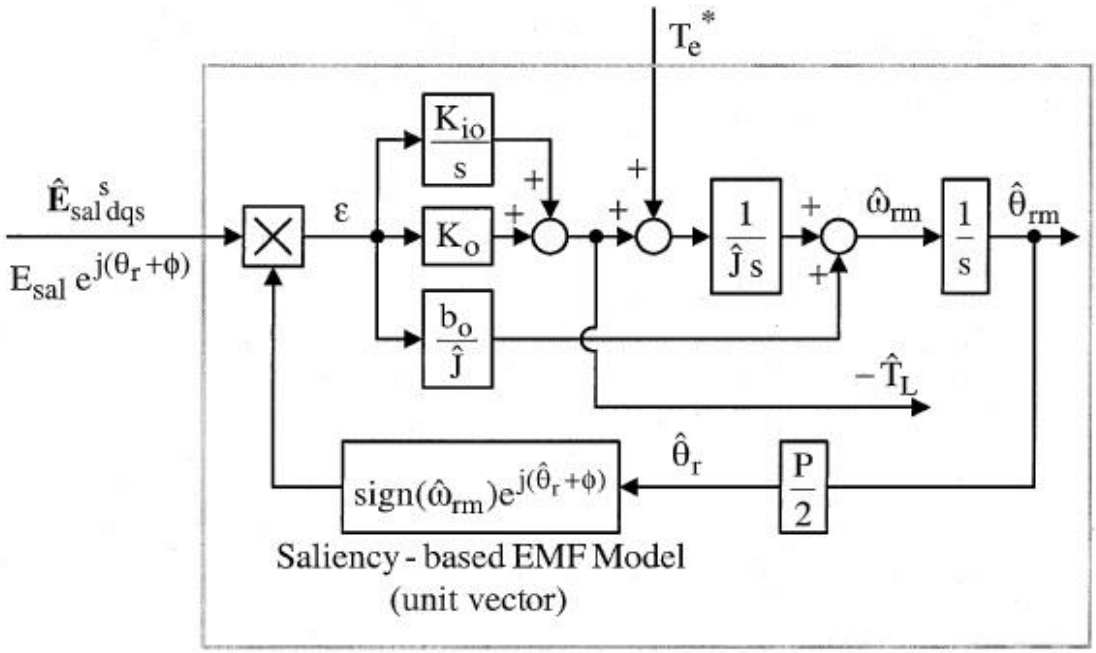

Fig. 2.10- Enhanced Luenberger style back-EMF tracking observer [22]

$$\hat{E}^{s}_{sal\_dqs} = \hat{E}^{s}_{sal}\, e^{\,j\theta_r + \pi/2} = \hat{E}_{sal}\begin{bmatrix} -\sin\theta_r \\ \cos\theta_r \end{bmatrix} \tag{2-29}$$

$$\varepsilon = \omega_r \left|\hat{E}_{sal}\right| \sin(\theta_r - \hat{\theta}_r) \tag{2-30}$$

Kim compared the position estimate results between the different mentioned methods (arctangent, state filter and enhanced Luenberger style observer) [2, 22]. It is worth noticing that when using the arctangent method the estimate position results in a noisy signal which means a remarkable position error (Fig. 2.11). On the other hand, filtering the noise would cause a lag on the estimate which is the case of the state filter that presents some lag in the position estimate (Fig. 2.12) although no noise at all. Lastly, Fig. 2.13 shows the performance of the observer in regards to the position estimate which contains the advantages of both previous methods.

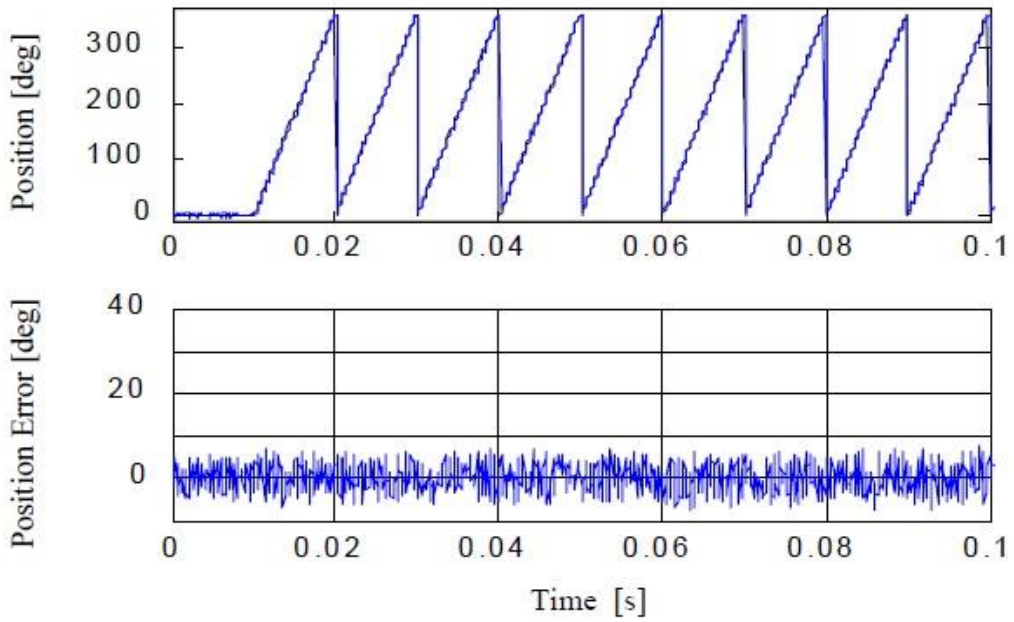

Fig. 2.11- Position estimate and simulated position (top) and position error (bottom) using the arctangent method [2]

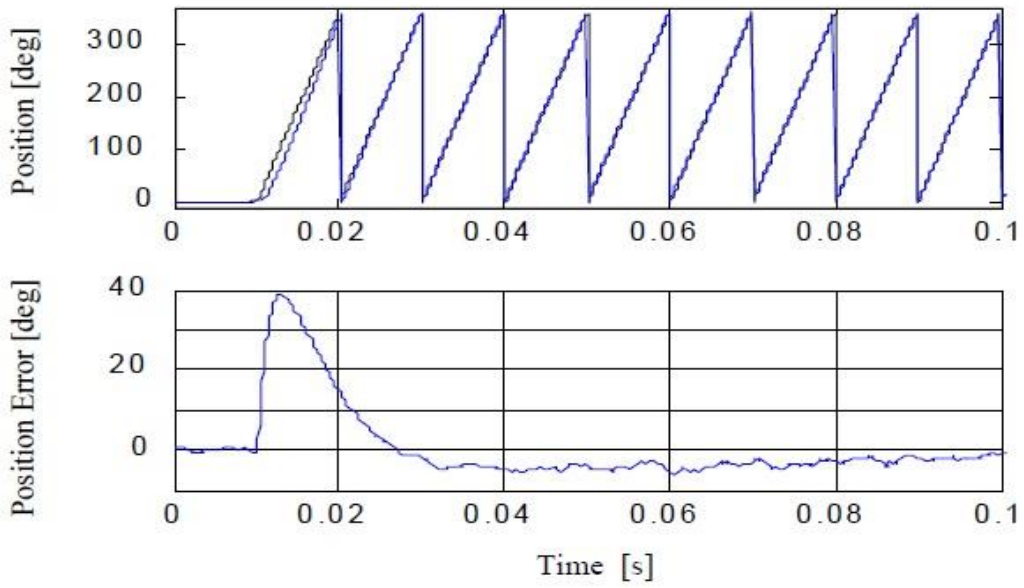

Fig. 2.12- Position estimate and simulated position (top) and position error (bottom) using the state filter method [2]

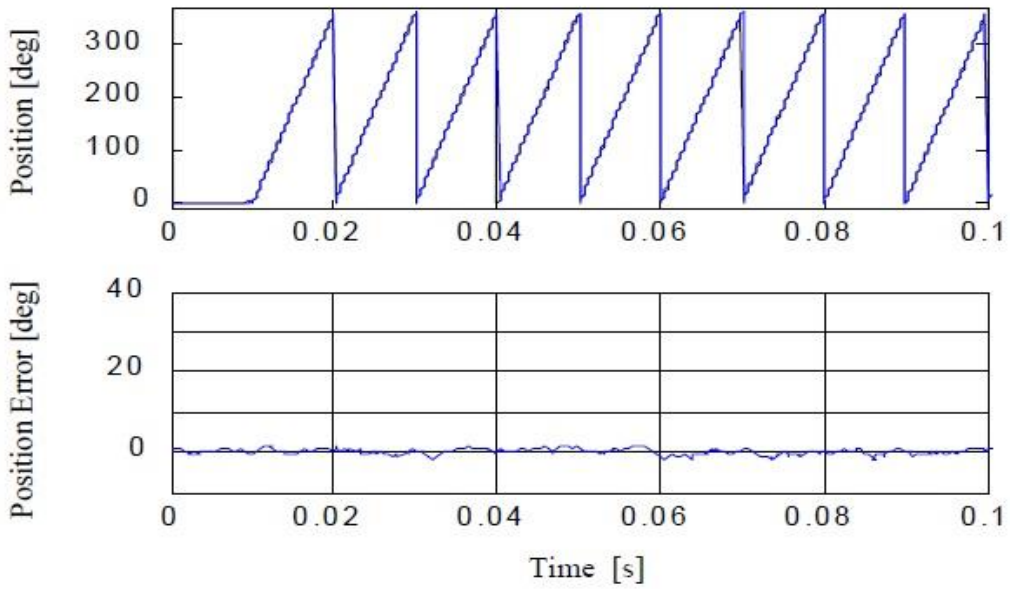

Fig. 2.13- Position estimate and simulated position (top) and position error (bottom) using the observer method [2]

In addition to Kim's work [2], Hejny [4] implemented both the saliency back-EMF filter and the enhanced Luenberger style observer in the discrete time and analyzed the harmonics caused by the inverter and the back-EMF when using the latter method. The remaining inverter harmonics affect the estimated values of position and speed especially at low speeds, and the velocity is the most sensitive one since it is not inherently low-pass filtered. Hejny proposes in this case adding an enhanced Luenberger style observer in cascade with the saliency back-EMF tracking observer. This approach (Fig. 2.14) filters out the harmonics in the estimated velocity without compromising the performance of the observer as it still has zero-lag in the estimated variables.

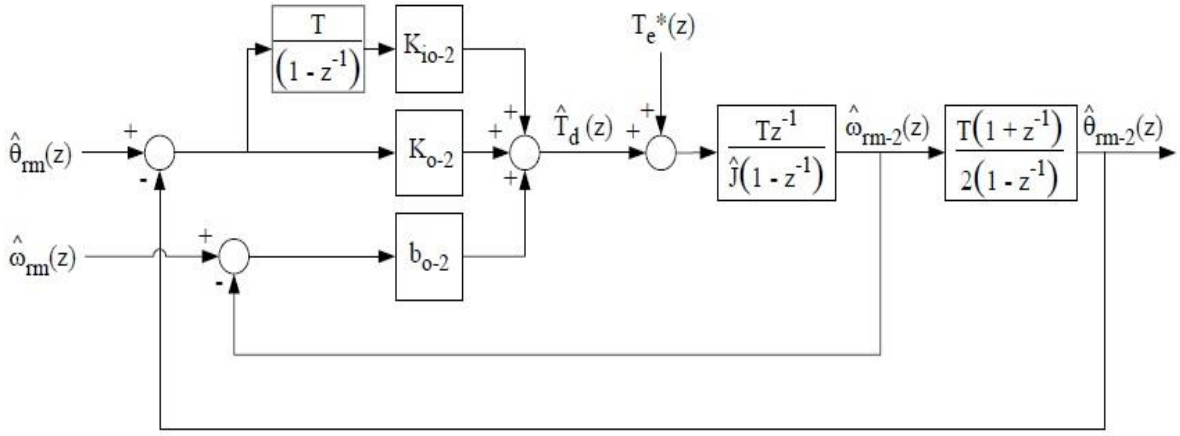

Fig. 2.14- Discrete time cascaded enhanced Luenberger style [4]

In [24] a new topology of a back-EMF observer is presented which consists in a quadrature phase-locked loop (PLL) with an adaptive notch filter (ANF) for a sliding mode observer (Fig. 2.15). This method compensates the harmonics in the back-EMF reducing the resulting error on the position estimate. The performance of this method is tested on an IPMSM machine (Fig. 2.16), the maximum position error is therefore reduced to 0.03π with the ANF.

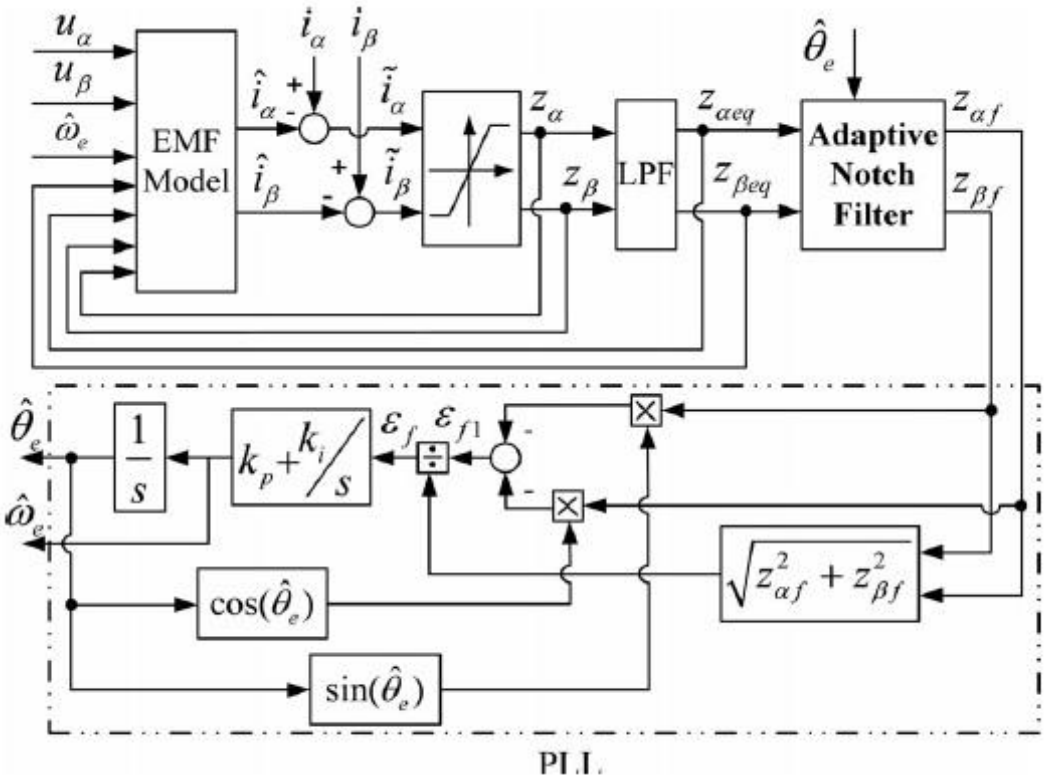

Fig. 2.15- Quadrature PLL with an ANF sliding mode observer [24]

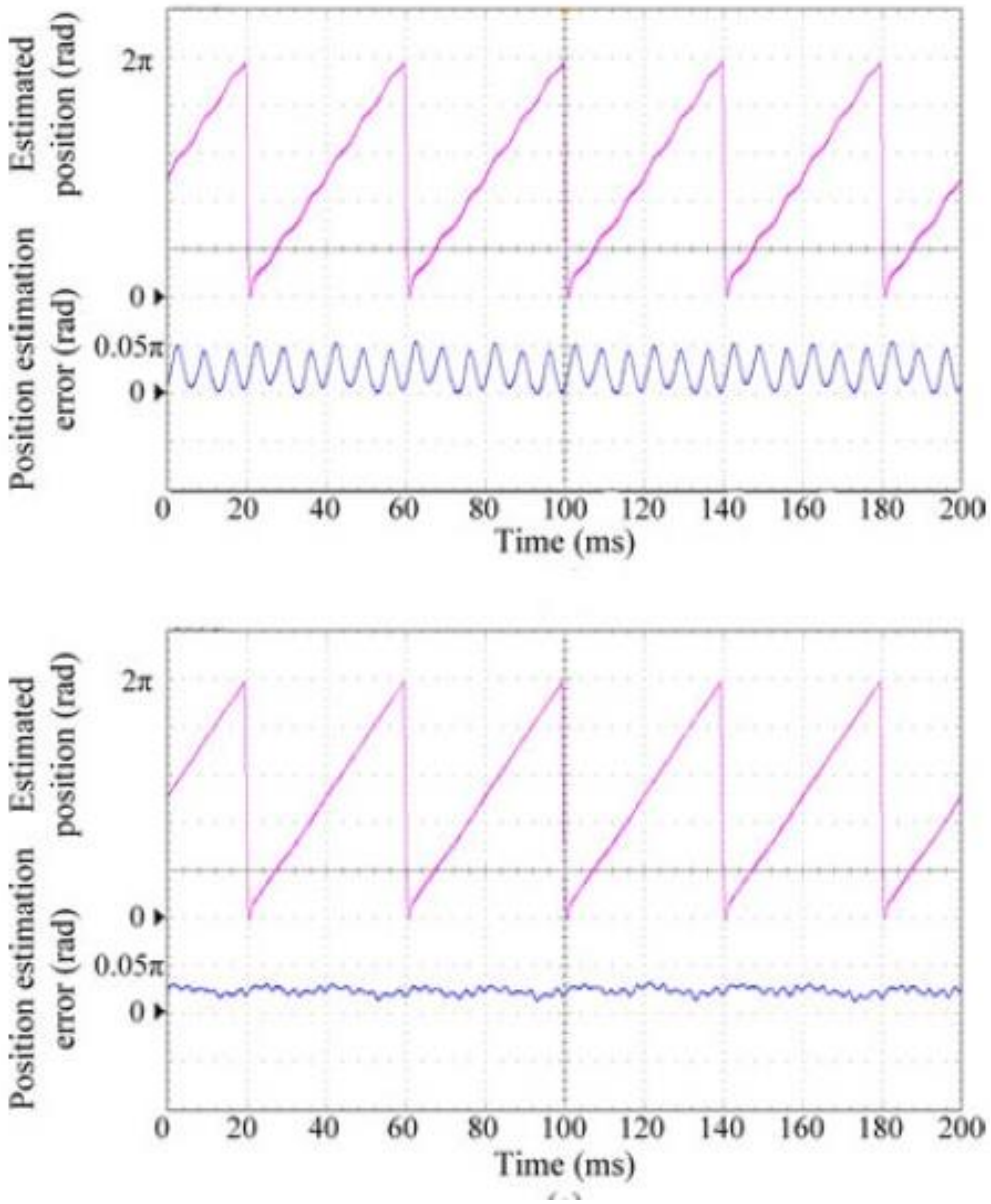

Fig. 2.16- Experimental comparison of position estimation error at 500 r/min and 50% rated load (7N-m), without using the ANF (upper plot) and using it (lower plot) [24]

2.4 Hybrid Self-Sensing Methods for Zero-to-Low Speeds and High Speeds

Knowing the limitations of back-EMF tracking at low speed and the effectiveness of HF injection methods within that range, some papers [25, 26] propose a hybrid self-sensing method combining the previous two. In [25] a rotating voltage injection method is used for the low speed range using a band-pass filter and synchronous-frame filtering in the demodulation process, the remaining current signal containing the position information is put into a Luenberger-style observer that allows getting both the position and the velocity estimates. In the case of the medium-to-high speed range back-EMF tracking is utilized. By means of a state filter the back-EMF is estimated, the position and velocity estimates are got through a Luenberger-style observer which has the back-EMF estimate as the input variable. The challenging part is how to switch from one operating mode to the other. This paper proposes a method to determine the transition region by looking at the harmonic content of the current reference. In doing so, the harmonic content of the q-axis reference current is analyzed as a function of the speed and for different observer bandwidths. Afterwards, the threshold value must be determined to switch from one mode to the other. Fig. 2.17 shows the performance of the self-sensing method with a speed profile from -60 to 60Hz showing a transition between the two different estimation methods.

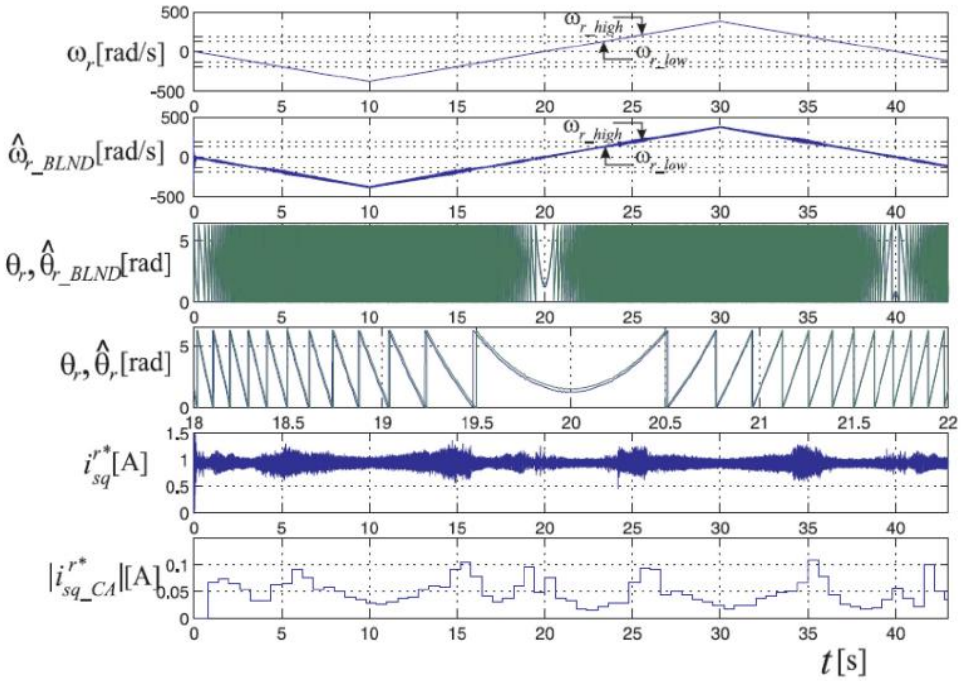

Fig. 2.17- Self-sensing control for the following speed range (−60Hz- 60 Hz): rotor speeds (ω_r, $\hat{\omega}_{r\_BLD}$), rotor positions (θ_r ,$\hat{\theta}_{r\_BLD}$), current reference (i_{sq}^{r*}) and rms AC content $\left| i_{sq}^{r*} \right|$ [25]

In [26], another hybrid self-sensing method is presented. In this case, a HF voltage signal is injected in the d-axis to track the position and speed at low speeds (Fig. 2.18), in order to estimate the position of the rotor an observer is used. Furthermore, this paper uses an EMF-based sliding mode observer with a PLL to estimate position at high speeds (Fig. 2.19).

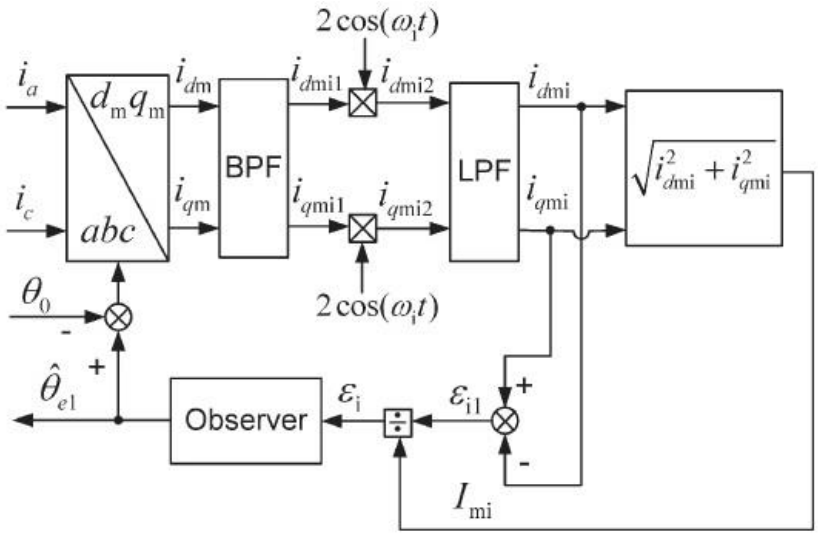

Fig. 2.18- Rotor position estimation scheme for low speeds [26]

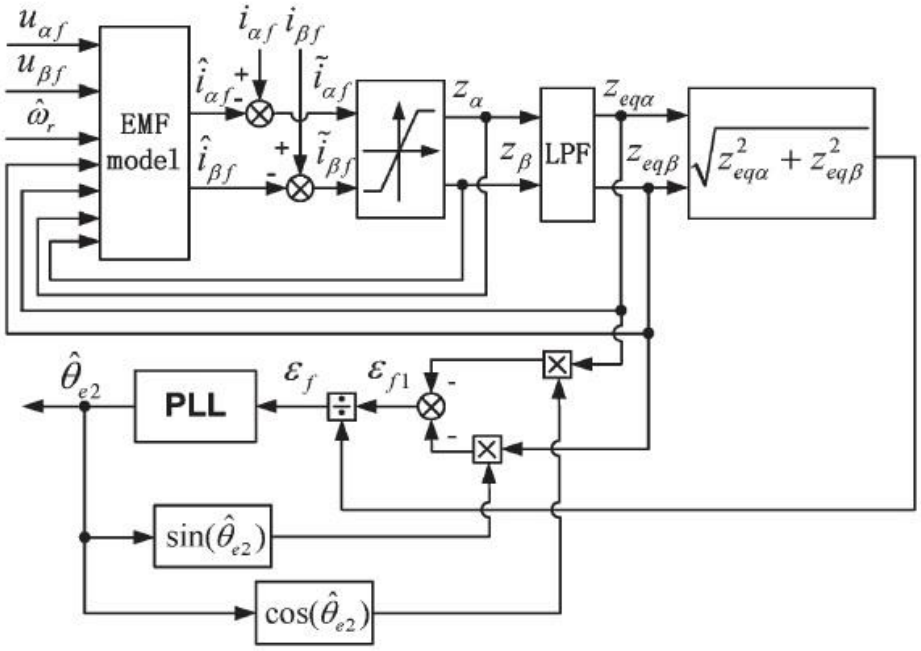

Fig. 2.19- Rotor position estimation scheme for high speeds [26]

Some experimental results are presented in Fig. 2.20 when the motor is run from 0 to 400r/min at rated load. From the experimental results it is concluded that this hybrid self-sensing method is more robust at high speeds.

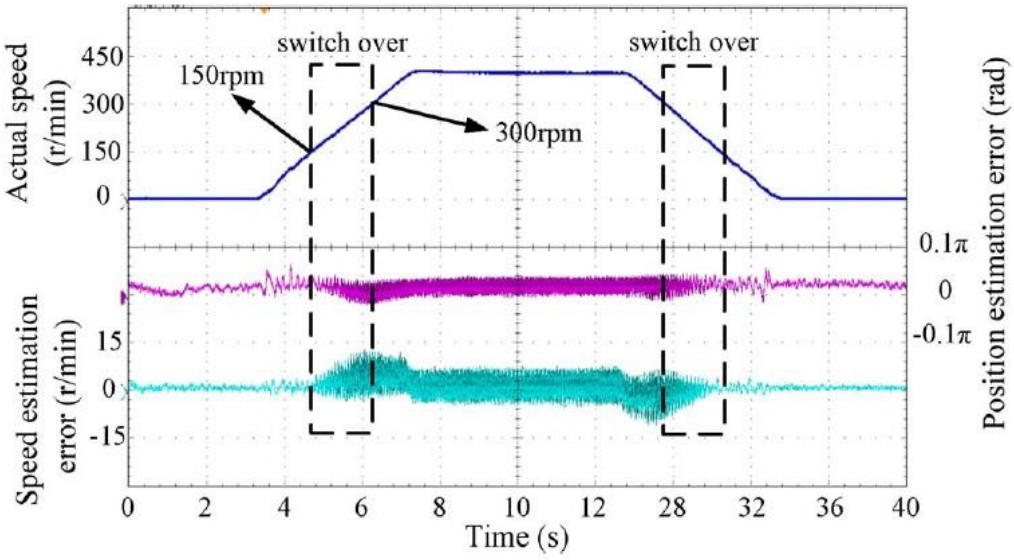

Fig. 2.20- Position and speed estimation error during the switch-over area from 0 to 400 r/min at rated load [26]

In Veltman's patent [27] whose low-speed method will be implemented in this thesis, a self-sensing approach is claimed to work for the whole speed range by using what it is called flux-tracking at high speeds and at zero-to-low speeds.

2.5 Flux Tracking Self-Sensing

Veltman proposes in his patent a self-sensing methodology to estimate position and velocity at both zero-to-low speeds and high speeds. The methodology presented is known as "Flux tracking".

This methodology involves tracking the PM flux linkage vector at high speeds and tracking the back-emf at zero-to-low speeds.

2.5.1 Flux Tracking at High Speeds

What Veltman does in his patent for the high speeds range is solving the motor (1-31) for the flux by substituting the back-EMF term by (1-32), resulting in the following (1-33).

$$\vec{u}=R\cdot\vec{i}+L\frac{d\vec{i}}{dt}+\vec{e} \tag{2-31}$$

$$\vec{e}=\frac{d\vec{\Psi}_m}{dt} \tag{2-32}$$

$$\vec{\Psi}_m=\int(u-R\cdot i)dt-L\cdot i \tag{2-33}$$

To remove the integral in (1-33), the patent multiplies both sides of the equation by the transfer function of a high-pass filter as can be seen in (1-34), where T is the time constant of the high-pass filter. When the integrator is multiplied by the high-pass filter the result is a low-pass filter. This way, the open-loop integration which is difficult to solve, is now avoided. It must be noticed that the angle of the estimated flux is displaced with the phase angle of the high-pass filter and must be corrected during the implementation of the method. The patent states that for positive ω values the phase error may be written as in (1-35).

$$\hat{\Psi}=\frac{sT}{1+sT}\cdot\Psi_m=\frac{T}{1+sT}\cdot(u-i\cdot R)-\frac{sT}{1+sT}\cdot i\cdot L \tag{2-34}$$

$$\phi=\frac{\pi}{2}-\arctan(\omega\cdot T) \tag{2-35}$$

The estimated flux in the stationary reference frame is rotated into the synchronous reference frame. If estimated correctly, all the flux would be on the d-axis and none in the q-axis. By means of the arctangent it can be determined the flux estimation error and this error signal is input into a PPL which will ultimately estimate the velocity and the position. Fig. 2.21 shows a block diagram of the invention method proposed in the patent and that ultimately is claimed to estimate velocity and position both at zero-to-low speeds and high speeds.

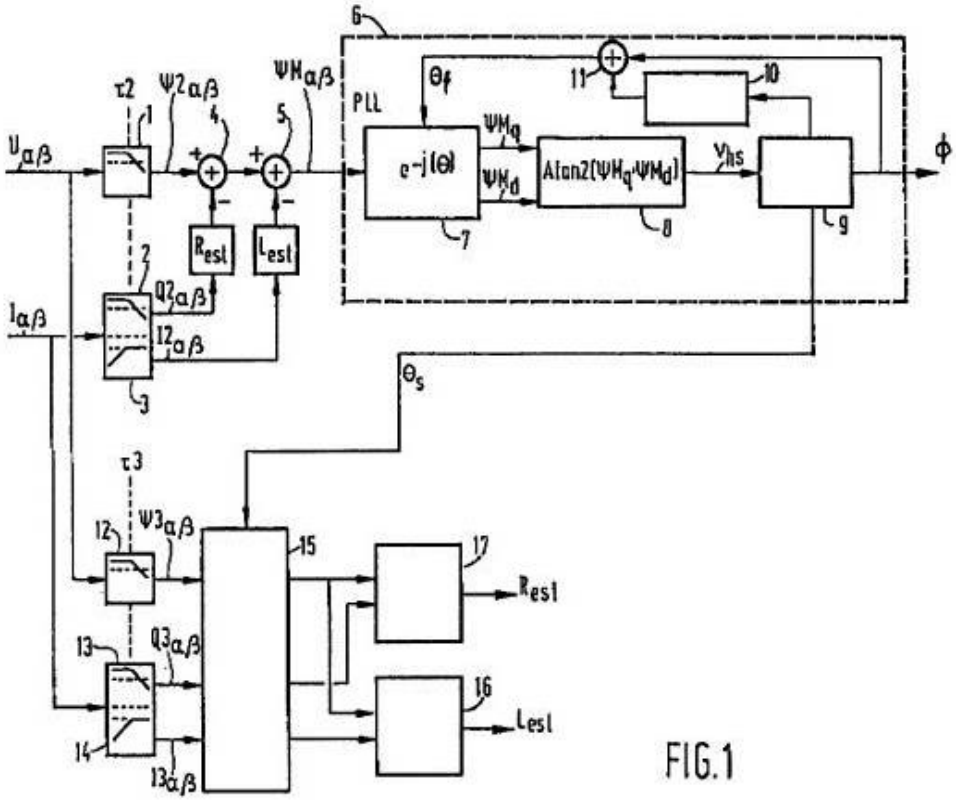

Fig. 2.21- High-speeds control scheme [27]

2.5.2 Flux Tracking at Zero-to-low Speeds

The patent estimates the back-EMF using the current and voltage measurements in the stationary reference frame. Being aware of the issues regarding back-EMF tracking at very low and zero speeds, Veltman suggests pulsing the controlling current on and off so during the on-current periods some back-EMF would be induced and may be tracked. This would make the rotor to oscillate around a fixed position if working at zero speeds. In order to accomplish this, the estimated back-EMF in the stationary reference frame is transformed into the rotor reference frame, where if estimated correctly, all of it should be on the q-axis and none on the d-axis. The arctangent is again used to calculate the resulting error of the estimation (1-36) and the PLL to get the position and velocity estimate.

Veltman shows in his patent a block diagram of the PLL used in his invention (Fig. 2.22) which he claims to use at both zero-to-low speeds and high speeds by switching the input. All that he says about the PLL is that in pulsed operation mode the pass-band of the PLL loop filter has to be decreased as well as the order of the PLL.

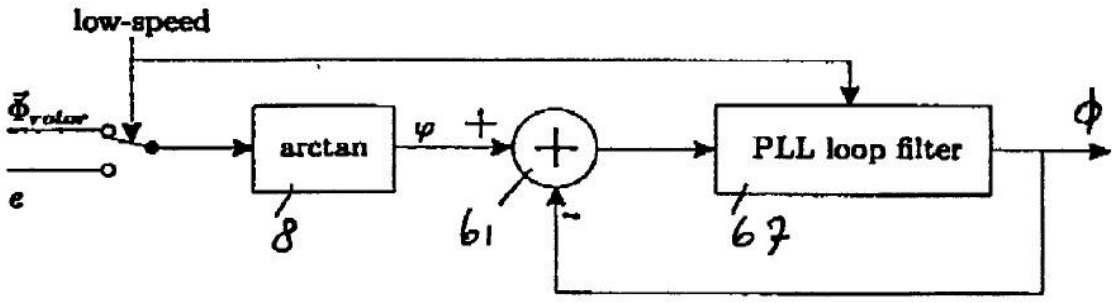

Fig. 2.22- Block diagram of a switchable input PLL for high speeds and zero-to-low speeds [27]

$$\phi = \arctan\left(\frac{\hat{E}_q}{\hat{E}_d}\right) \quad (2\text{-}36)$$

2.5.2.1 Pulsating the Torque to Zero to Measure Back-EMF

One of the key points of Flux tracking is sense back-EMF at zero-to-low speeds so it can be tracked. In that regard, the patent only claims that during the pulsating mode, during the off time the impedance voltage drop is guaranteed to be 0V since the controller current is pulsed off. During this period the measured voltage would be the back-EMF not requiring impedance compensation and therefore not disturbing the measured induced voltage.

2.6 Research Opportunity

There is a lack of information about this methodology since many issues are not discussed in the patent. The patent does not say the frequency at the current is being pulsed, but that it is done at low frequency. It is not documented what back-EMF magnitude is induced so that it can be tracked in the low speed range. No simulation nor experimental results are shown in the patent either. There is not any other documentation published yet besides this patent, and therefore this is where there is an opportunity of research and where this thesis is focused on, that is implementing and documenting a simulation model for self-sensing position and velocity estimation for zero-to-low speeds and evaluating its performance. Furthermore, this thesis will analyze the limitations and

capabilities of this approach via analyzing the dynamic stiffness and the parameter sensitivity.

Chapter 3

Development of a Simulation Model for Flux Tracking at Zero-to-Low Speeds

This second chapter presents a simulation model based on the method introduced by Veltman [27] and presents a better understanding and documented analysis of the patented methodology that has not been done yet. The simulation model has been performed using the *Simulink* software from MATLAB.

The parameters of the SPMSM model used in the simulation are shown in Table 3.1.

Table. 3. 1- SPMSM parameters

Parameter	Value
Series Inductance (L_s)	0.002[H]
Series Resistance (R_s)	0.9[Ω]
Number of Poles (P)	6
Inertia (J)	2 x 10^{-4} [Kg-m^2]
PM Flux Linkage (λ_{PM})	0.0677[V-s]
Nominal Torque (T_N)	5[N-m]

3.1 Physical Machine Model

The first part of developing a simulation model is to create the electrical model of a SPMSM using the equations in the stationary reference frame (1-17) and (1-18). The implementation of the machine equations is shown in the block diagram of Fig. 3.1

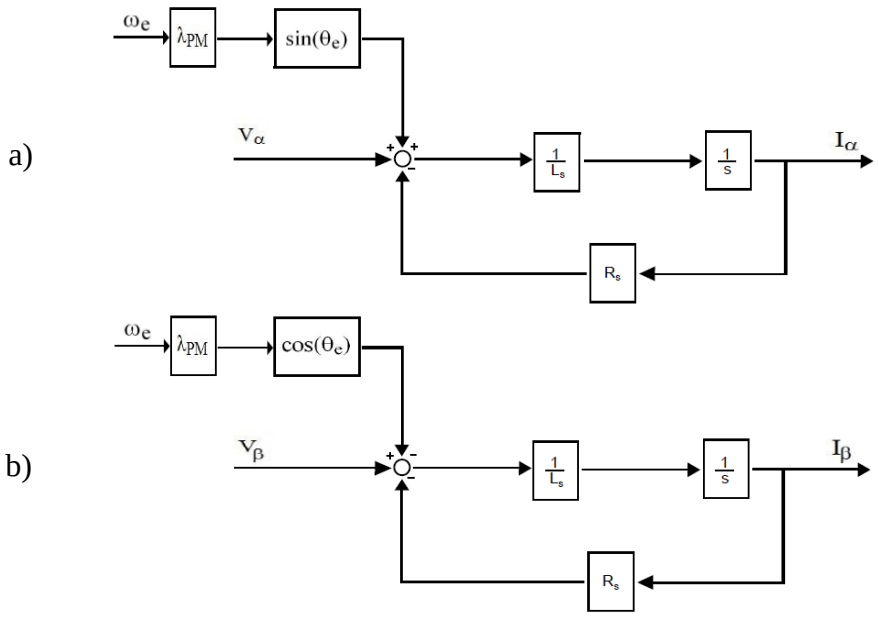

Fig. 3.1- Electrical model of a PMSM in the stationary reference frame: a) d-axis, b) q-axis

3.2 Current Control Loop

Once the machine model in the stationary reference frame is developed, the next step is to close the current control loop. A block diagram of the current control loop is shown in Fig. 3.2.

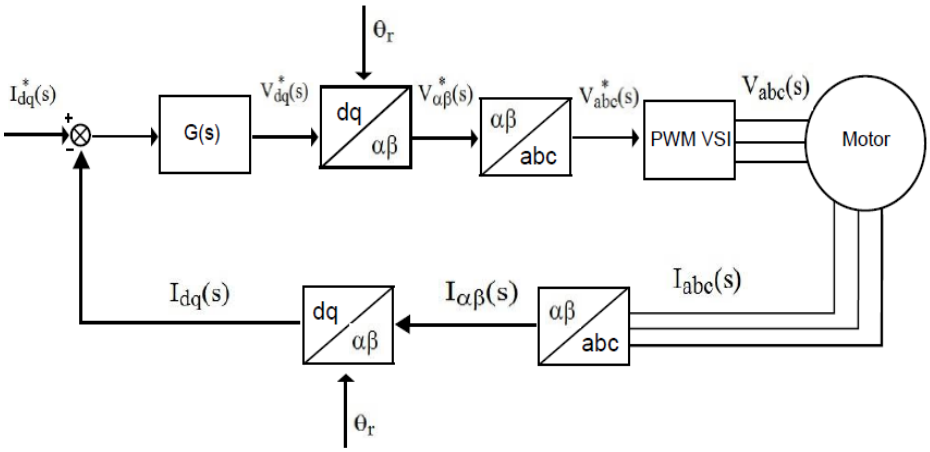

Fig. 3.2- Current Control Loop block diagram

This block diagram (Fig. 3.2) shows the current controller that drives the voltage source inverter (VSI) and ultimately the motor.

As the PMSM used for this simulation is an SPMSM the d-axis current in the synchronous reference frame will be set to zero at all times by the controller. This means that flux weakening is not implemented in the control. Both d and q current references go through the current controller which would generate a voltage reference to the inverter.

For the d and q axis current controllers (G(s)) PIs are used (Fig. 3.3). As mentioned before, the q-axis current will be the one in charge of producing torque and therefore, the d-axis current will be set to zero at all times by the controller. For the current controllers a bandwidth of 1000Hz is used. And they have been tuned by doing zero-pole cancellation. The gains of the controller are therefore obtained from (1-37) and (1-38).

Where 'bw' is the bandwidth of the current controller and 'L_s' and 'R_s' are the series stator inductance and resistance of the SPMSM respectively.

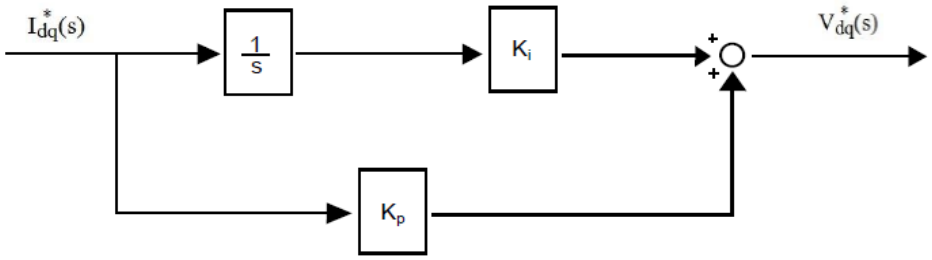

Fig. 3.3- PI Current controller block diagram

$$K_p = 2\pi \, bw \, L_s \tag{2-37}$$

$$K_i = \frac{R_s}{L_s} \tag{2-38}$$

3.3 Self-Sensing at Zero-to-low Speeds

This subsection explains the development of the self-sensing flux tracking methodology at zero-to-low speeds that Veltman claimed to use in his patent [27].

3.3.1 Pulsating the Torque to Zero to Measure Back-EMF

As explained in the state-of-the-art review chapter Veltman claims to use a pulsating current to induce back-EMF at low speeds. Based on the interpretation of his patent: “In pulsed mode operation the current is switched on and off at a low frequency” the q-axis current of the controller (that produces the torque) is pulsed on and off to make the rotor to oscillate around its actual position (Fig. 3.4). In order to do that a switch will switch it on and off depending on the output of a square waveform of the pulsating frequency (f_p) at which the controller current is being pulsed. The duty cycle of the square waveform is 50%.

This way, at low speeds and even at standstill the back-EMF magnitude induced is big enough to be tracked and allows estimating rotor position and velocity accurately.

Fig. 3.5 explains through a vector diagram the back-EMF tracking when pulsing the current on and off. In the off period the measured voltage will equal the back-EMF, whereas when the current is on, it is a bit displaced due to the voltage drop in the impedance.

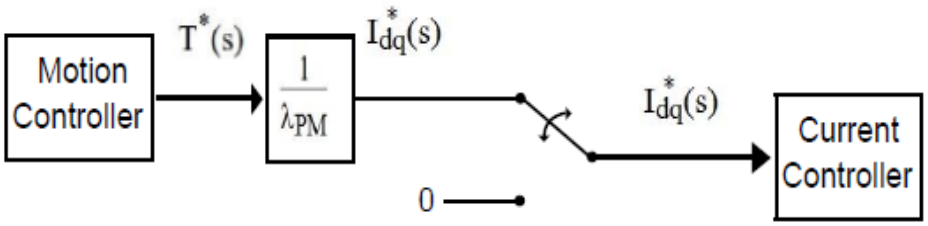

Fig. 3.4- Block diagram of the on and off pulsation of the torque

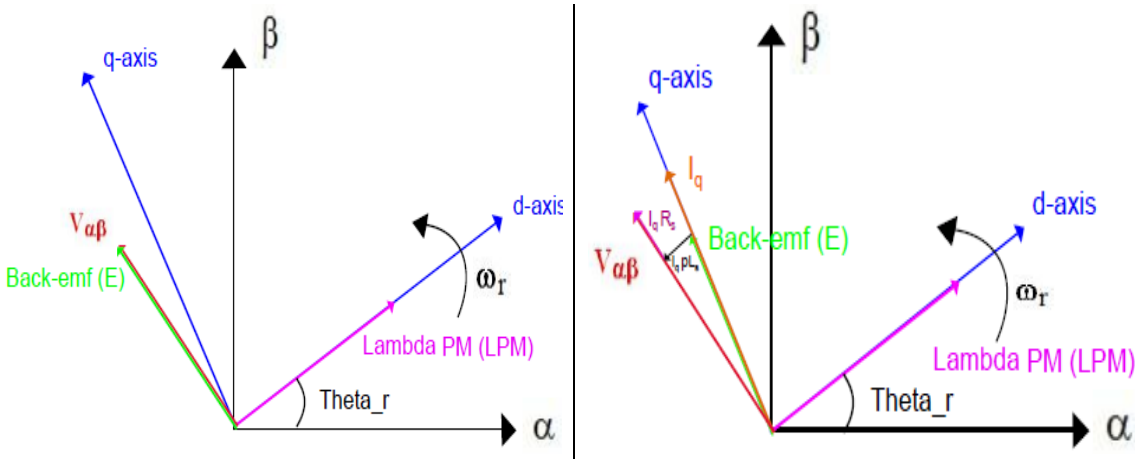

Fig. 3.5- Vector diagram when the current is pulsed off (left) and when it is pulsed on (right).

The magnitude of back-EMF that is induced is shown in Fig. 3.6, when the q-axis controller current is pulsed on and off for different pulsing frequencies (25, 50, and

100Hz). It can be appreciated that as the pulsing frequency is increased, the amount of back-EMF induced is decreased. This occurs because increasing the pulsing frequency means reducing the time the rotor is allowed to rotate and therefore means also reducing the rotor speed. This is also shown in more detail in Fig. 3.7 and 3.8

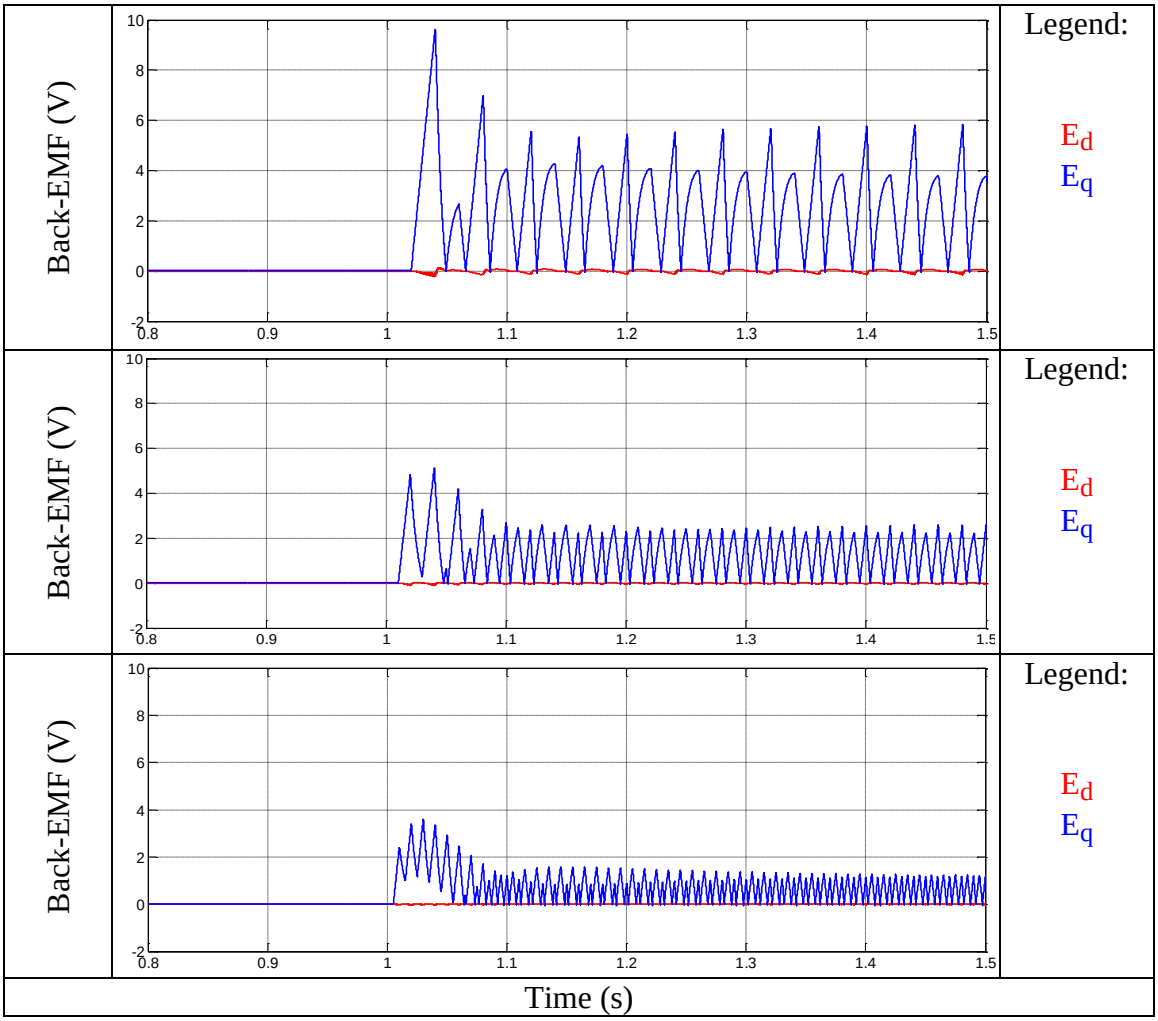

Fig. 3.6- Back-EMF signal in the synchronous reference with a load torque (T_L) of 0.5 N-m(0.1pu) and for different pulsing frequencies (f_p): From top to bottom: f_p= 25Hz, f_p= 50Hz, f_p= 100Hz

Fig. 3.7 and Fig. 3.8 show the dependency of the rotor position, rotor speed and back-EMF on different pulsing frequencies and for a load torque (T_L) of 0.5 (0.1pu) and 1N-m (0.2pu) respectively. It may be seen in Fig. 3.7 that for lower pulsing frequencies the rotor goes further in position and speed and therefore more back-EMF is induced, whereas if the pulsing frequency is increased the rotor oscillations are much smaller in magnitude and therefore less back-EMF would be induced. Moreover, the load torque (T_L) also plays an important role in this matter. The magnitude of rotor position, velocity and back-EMF increase as the T_L does.

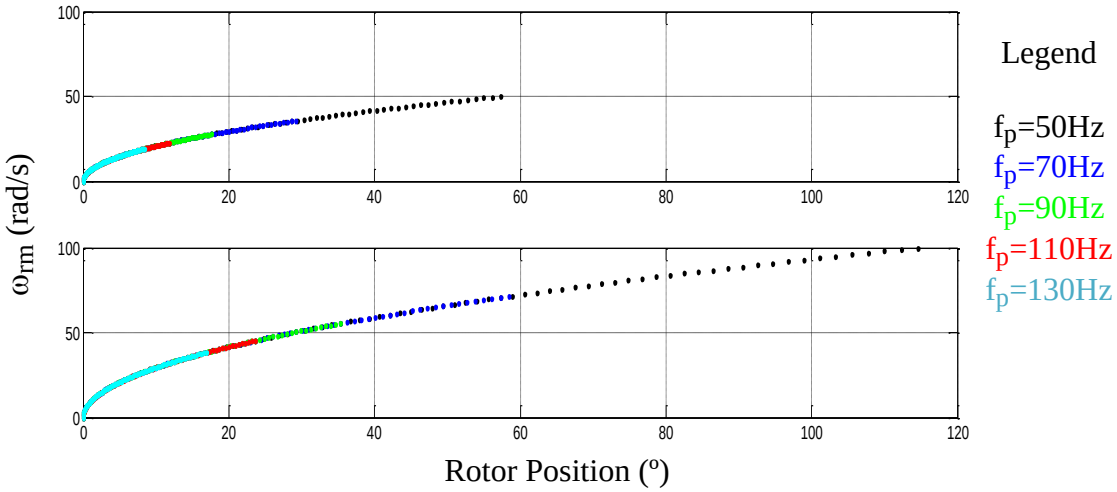

Fig. 3.7- Rotor speed (ω_{rm}) at different pulsing frequencies and load torque values.

For the upper plot T_L=0.5N-m (0.1pu), and for the lower one T_L=1N-m (0.2pu)

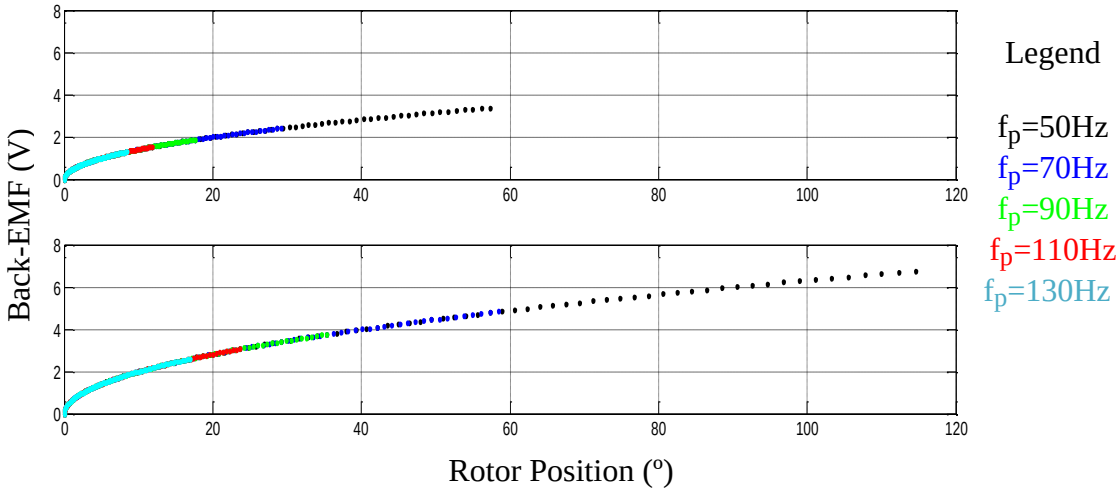

Fig. 3.8- Back-EMF for different pulsing frequencies and load torque values.

For the upper plot T_L=0.5N-m (0.1pu), and for the lower one T_L=1N-m (0.2pu)

3.3.2 Position and velocity estimation

To estimate the position and speed, the back-EMF must be known. From the measured stator voltages and currents in the stationary reference frame the back-EMF can be calculated as shown in Fig. 3.9. The resultant back-EMF in the stationary reference frame is transformed into the estimated rotor reference where if estimated correctly, all the back-EMF should be on the estimated q-axis (Fig. 3.10), (Fig. 3.11). In Fig. 3.10 a counterclockwise direction of the rotor speed is considered whereas in Fig. 3.11 the rotor is supposed to spin clockwise. The speed direction must be taken into account when calculating the back-EMF to know where the vector is placed in the estimated rotor reference frame. By using the arctangent method with the back-EMF in the synchronous

reference frame (1-36) and a Phase-locked loop (PLL) the position and speed are estimated.

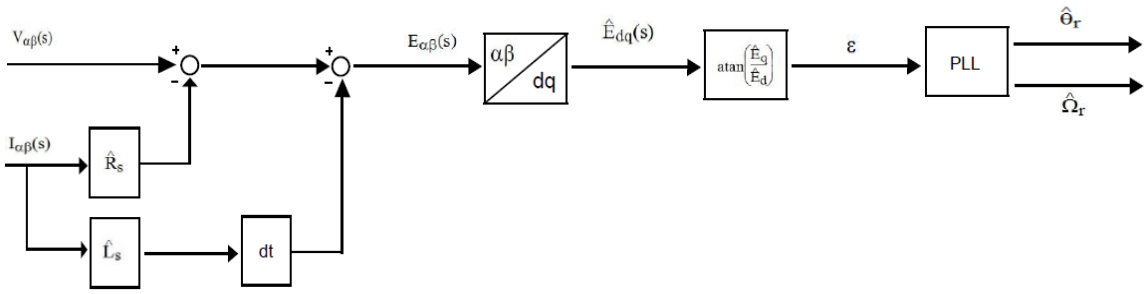

Fig. 3.9- Position and velocity estimation scheme

The PLL estimates the rotor position ($\hat{\theta}_r$) directly, by correcting the actual angle to the back-EMF one in the synchronous reference frame. That is why the speed direction must be taken into account to figure out the θ_r angle. By having a look at figures 3.10 and 3.11 it is deduced that for positive speeds (clockwise) $\pi/2$ are added to the back-EMF angle to get the rotor one; whereas for negative speeds the same angle ($\pi/2$) shall be substracted.

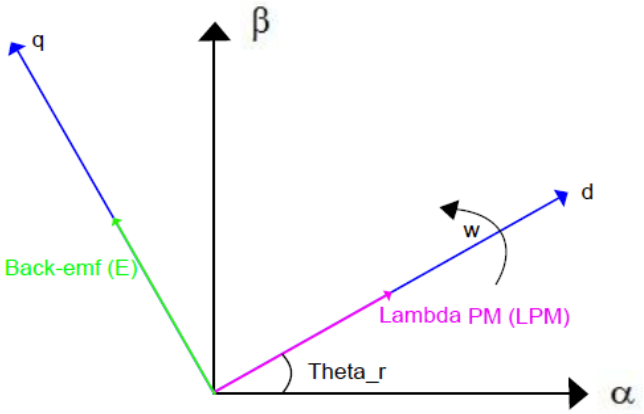

Fig. 3.10- Back-EMF and PM flux linkage on the rotor reference frame (counterclockwise speed direction)

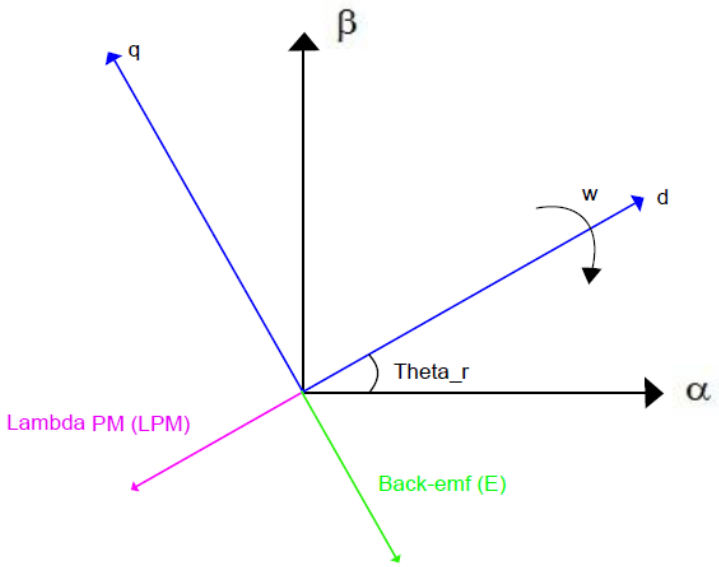

Fig. 3.11- Back-EMF and PM flux linkage on the rotor reference frame (clockwise speed direction)

3.3.3 Arctangent implementation

The arctangent method implemented presented some problems when the d-axis back-EMF component crosses zero, making the output to go up to $\pm\pi$ (Fig. 3.12). This has been corrected in the simulation by subtracting or adding $\pm\pi$ depending on the case (Fig. 3.13). Now the output of the arctangent does not have spikes every time the back-EMF d-axis component in the estimated reference frame ($\hat{E}_d$) crosses zero.

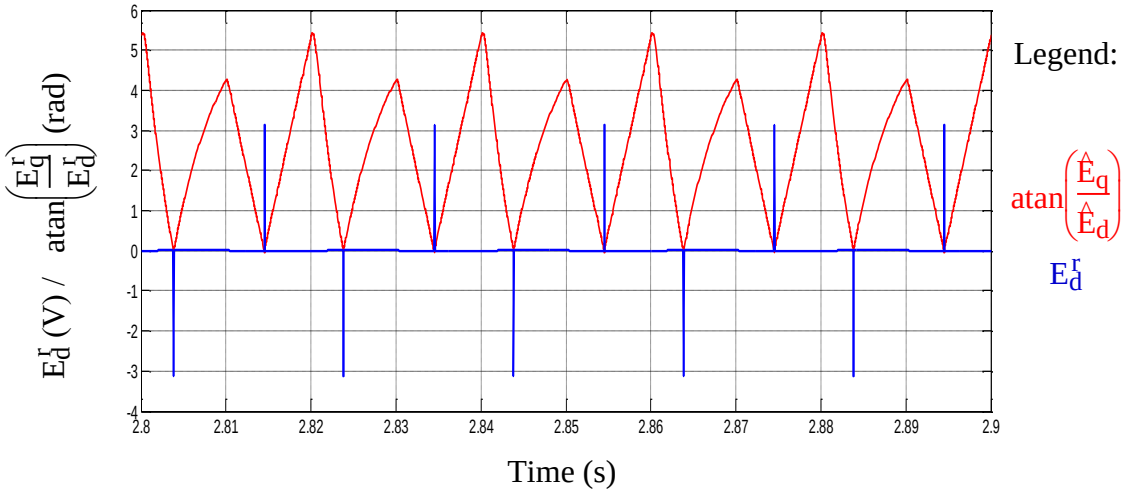

Fig. 3.12- D-axis Back-EMF component and arctangent output without correction

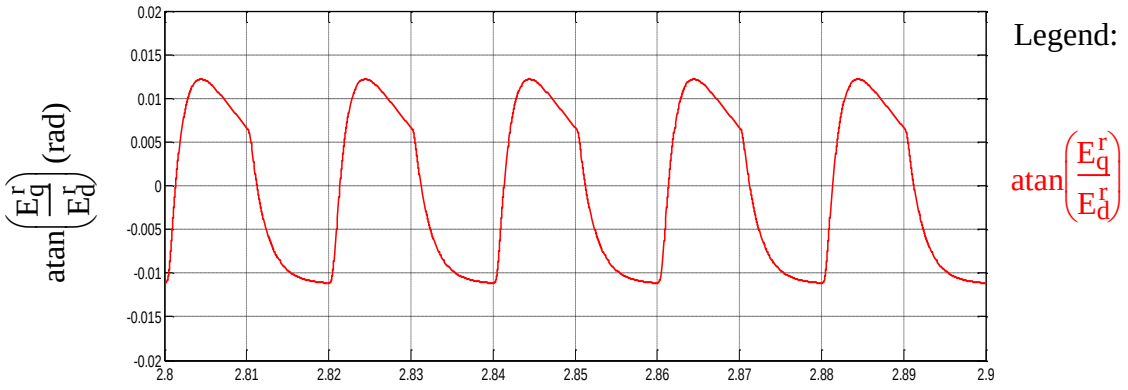

Fig. 3.13- Corrected arctangent output

3.3.4 Phase-Locked-Loop (PLL) implementation

For the Phase-Locked Loop, the PII topology presented in Fig. 3.14 is utilized. The bandwidth selected is 200Hz. This topology allows estimating velocity and position accurately as shown in the simulation results.

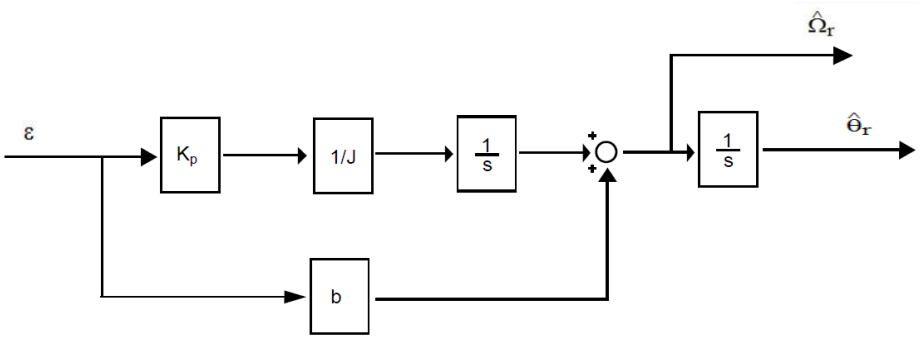

Fig. 3.14- Phase-Locked Loop Topology

The transfer function of this PLL is shown in (1-39).

$$\frac{\hat{\theta}}{\theta_{ref}} = \frac{\left(\frac{K_p}{sJ} + \frac{b}{J}\right)\frac{1}{s}}{1 + \left(\frac{K_p}{sJ} + \frac{b}{J}\right)\frac{1}{s}} \tag{1-39}$$

If (1-39) is multiplied by Js^2 on both the numerator and denominator the following transfer function is obtained (1-40).

$$\frac{\hat{\theta}}{\theta_{ref}} = \frac{bs + K_p}{Js^2 + bs + K_p} \tag{1-40}$$

This way, the gains (1-41) and (1-42) are calculated to achieve a specific bandwidth.

$$K_p = bw_1\, bw_2\, J \tag{1-41}$$

$$b = \left(bw_1 + bw_2\right) J \tag{1-42}$$

3.4 Motion controller

The last thing left to develop in the simulation model is the motion controller. The input of the motion controller is a commanded speed reference which will create an error term when the estimated speed is subtracted to it. This error signal will input the motion controller which generates a torque command directly proportional to the q-axis current in the synchronous reference frame (1-8), (Fig. 3.15).

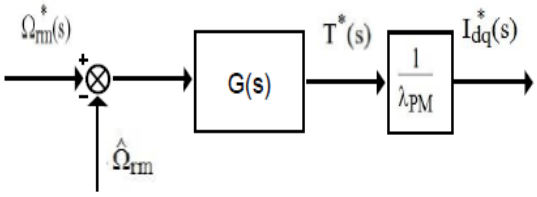

Fig. 3.15- Motion controller block diagram

The speed controller topology proposed is shown in Fig. 3.16 This topology presents zero steady-state error both in position and speed. The input 'ε' is the speed error term and $T^*(s)$ is the commanded torque. The gains of the controller are calculated as a function of the desired bandwidths. In Fig. 3.17 the physical meaning of the gains for the aforementioned speed controller is shown in a dynamic stiffness plot.

The transfer function related to Fig. 3.16 is shown in (1-43).

$$\left|\frac{T_d}{\omega}\right| = \frac{Js^3+b_as^2+K_{sa}s+K_{isa}}{s^2} \qquad (1\text{-}43)$$

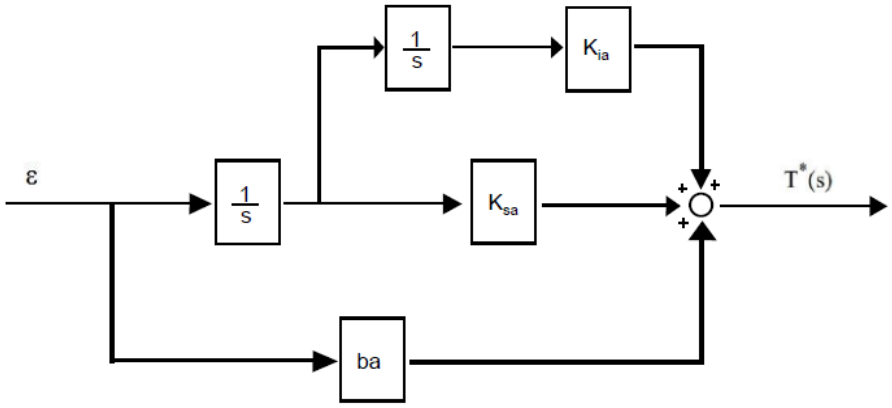

Fig. 3.16 Speed regulator block diagram

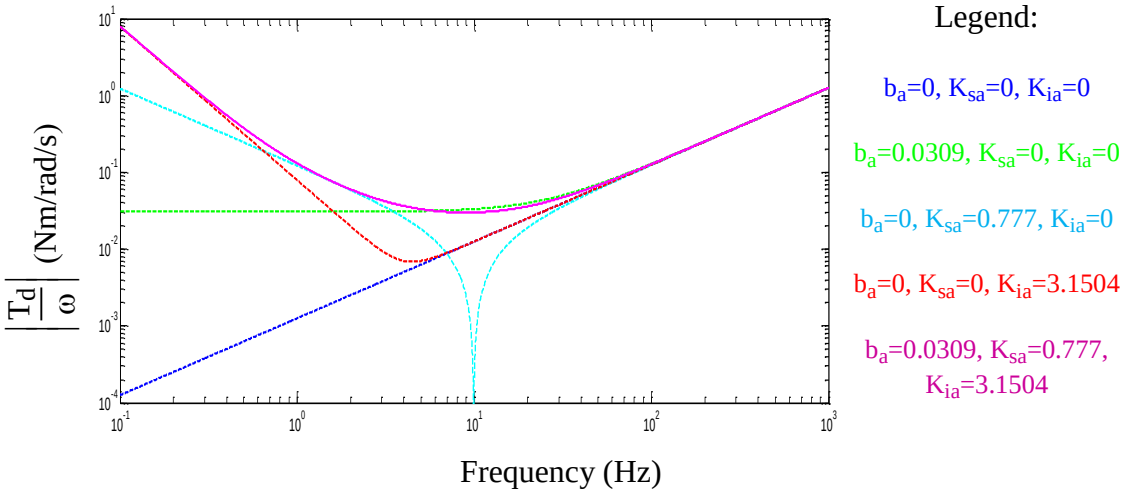

Fig. 3.17- Speed controller tuning via dynamic stiffness.

To tune up the motion controller, the location of the controller poles is determined to achieve having the different bandwidths. (1-44) to (1-46) show the location of the poles and (1-47) to (1-49) show how the motion controller gains are calculated for the desired poles location.

$$Z_1 = e^{-2\pi\, b_{w_1}\, T_s} \quad (1\text{-}44)$$

$$Z_2 = e^{-2\pi\, b_{w_2}\, T_s} \quad (1\text{-}45)$$

$$Z_3 = e^{-2\pi\, b_{w_3}\, T_s} \quad (1\text{-}46)$$

$$b_a = \frac{J}{T_s}\left(1 - Z_1 Z_2 Z_3\right) \tag{1-47}$$

$$K_{sa} = \frac{J}{T_s^2}\left(3 - 2\, b_a \frac{T_s}{J} - Z_1 Z_2 - Z_1 Z_3 - Z_2 Z_3\right) \tag{1-48}$$

$$K_{ia} = \frac{J}{T_s^3}\left(3 - b_a \frac{T_s}{J} - K_{sa} \frac{T_s^2}{J} - Z_1 - Z_2 - Z_3\right) \tag{1-49}$$

In this model the bandwidths used for the motion controller are b_{w1}=20Hz, b_{w2}=4Hz and b_{w1}=0.8Hz respectively. For these bandwidths the consequent values of the motion controller gains are: b_a=0.0309, K_{sa}=0.777, and K_{ia}=3.1504.

3.5 Summary

This chapter has presented the simulation model developed in Simulink. The first part that has been described is the implementation of the electrical machine model following the mathematical equations from (1-17) and (1-18).

Once the machine model is developed the close-loop current control is implemented using measured feedback for the transformations from stationary to synchronous reference frame and vice versa. For the current regulators PIs have been used and zero-pole cancellation has been done to achieve no error in steady state.

The next step that has been taken was the implementation of the flux-tracking self-sensing methodology first proposed by Veltman [27]. How the controller current is pulsed and the back-EMF generated for different pulsing frequencies has been addressed in this chapter.

Moreover, this chapter explains how the position and velocity are estimated by using the arctangent methodology and a Phase-Locked-Loop (PLL) that ultimately allows estimating those two variables accurately.

Lastly, the motion controller topology used is explained.

Chapter 4

Evaluation of Simulation of Flux Tracking at Zero-to-Low Speeds

This chapter evaluates the simulation model validity on the position and velocity estimation results under a different set of conditions (different pulsing frequencies, load torque values and speeds).

Furthermore, the simulation model is also evaluated via dynamic stiffness and parameter sensitivity analysis. This will contribute more knowledge about its limitations.

4.1 Position and Velocity Estimation Simulation results

In this section the simulation results obtained from the simulation model built in *Simulink* concerning both position and velocity estimation are presented under a set of different conditions involving different load torque values, different pulsing frequencies to pulse the controller current on and off, and eventually different machine speeds (0 rad/s and 10 rad/s). The pulsing frequencies considered in these tests are 30, 50 and 70Hz. There is not

a lower limit of frequency as the more time the rotor oscillates the more back-EMF that is induced. Nevertheless depending on the application it may not be acceptable allowing the rotor to rotate widely around its position. As for the upper limit, the back-EMF magnitude induced has to be enough to allow the tracking.

4.1.1 Position estimation at zero speed

The following figures (Fig. 4.1-Fig. 4.3) show the position estimation and the respective error at zero speed for different pulsing frequencies (30, 50, 70Hz) and different load torque values (0.2, 0.5, and 1N-m). A sinusoidal torque disturbance of 0.1 N-m is introduced as a perturbation at 3.5s to see how well the system responds to such a perturbation in the load.

It is concluded from these simulation results that when increasing the load torque, the pulsing frequency should be increased consequently to reduce the error in the position estimation. In the worst case of the analyzed ones, the position error is around 0.03 electrical radians approximately which equals to 1.72 electrical degrees. It is appreciated that the model is capable of producing very good position estimates even when the load disturbance is applied to the machine.

The limitation of this model is that some T_L is needed in order for the motor to be able to produce pulsating torque and therefore, generate back-EMF. Fig. 4.4 shows the position estimation as well as the back-EMF in the synchronous reference frame at zero speed and T_L=0N-m. At 3.5 seconds a sinusoidal torque disturbance is introduced

allowing that way to have some back-EMF and allowing the tracking of the position and velocity. Therefore, injecting a small sinusoidal torque disturbance is required for this methodology to work if T_L=0N-m.

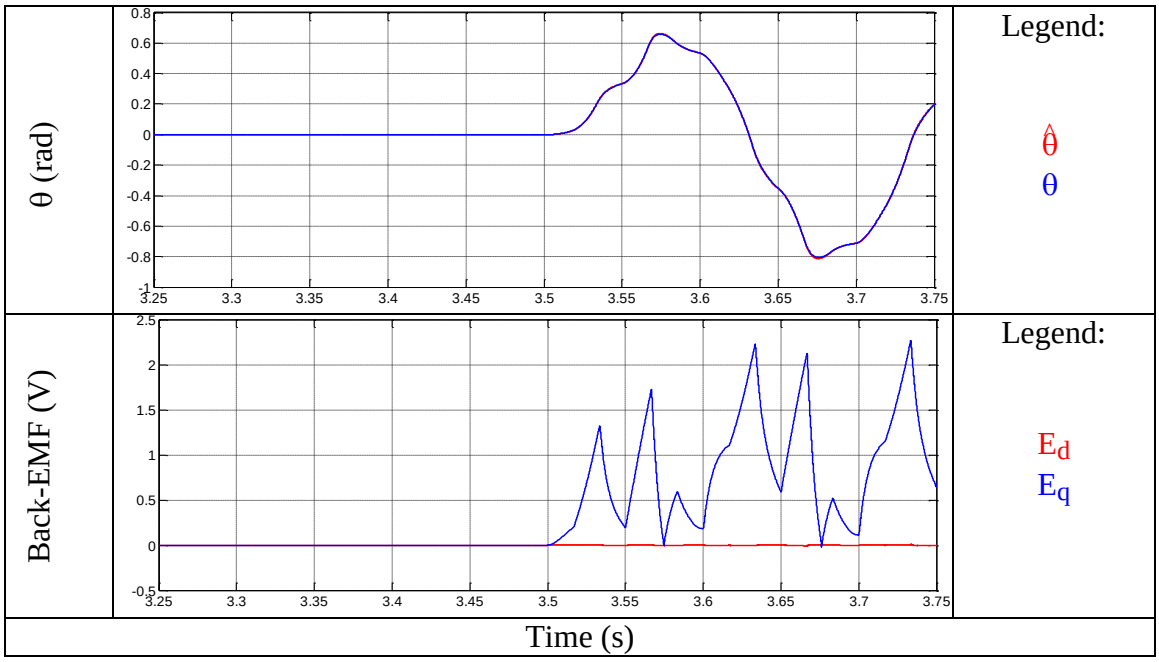

Fig. 4.4- Position estimation and back-EMF at 30Hz pulsating frequency, at zero speed (ω_{rm} = 0rad/s) and for different load torque T_L= 0N-m

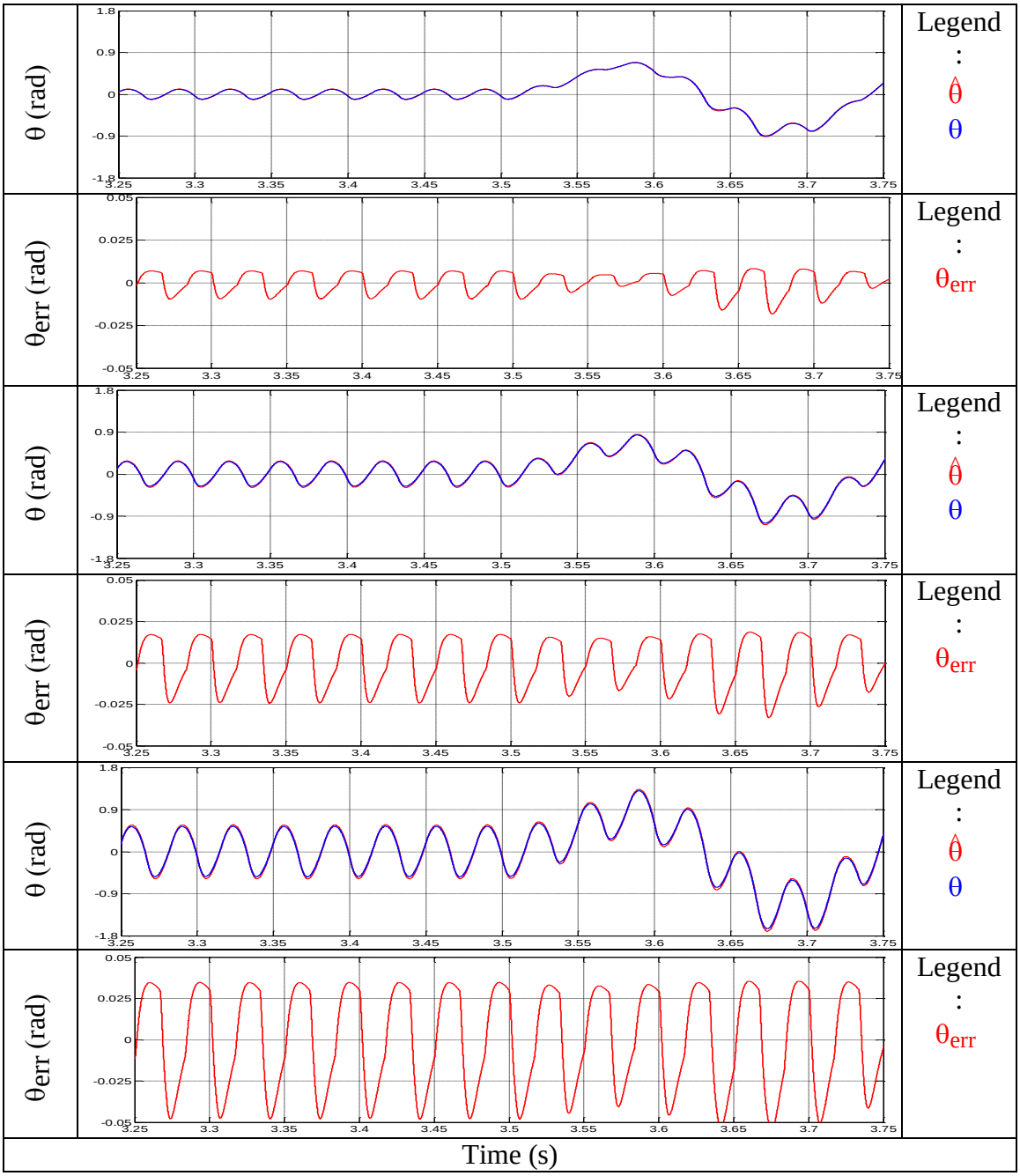

Fig. 4.1- Position estimation and position estimation error at 30Hz pulsating frequency, at zero speed (ω_{rm} = 0rad/s) and for different load torque values (From top to bottom: T_L= 0.2N-m (0.04pu), T_L= 0.5N-m (0.1pu), T_L= 1N-m (0.2pu))

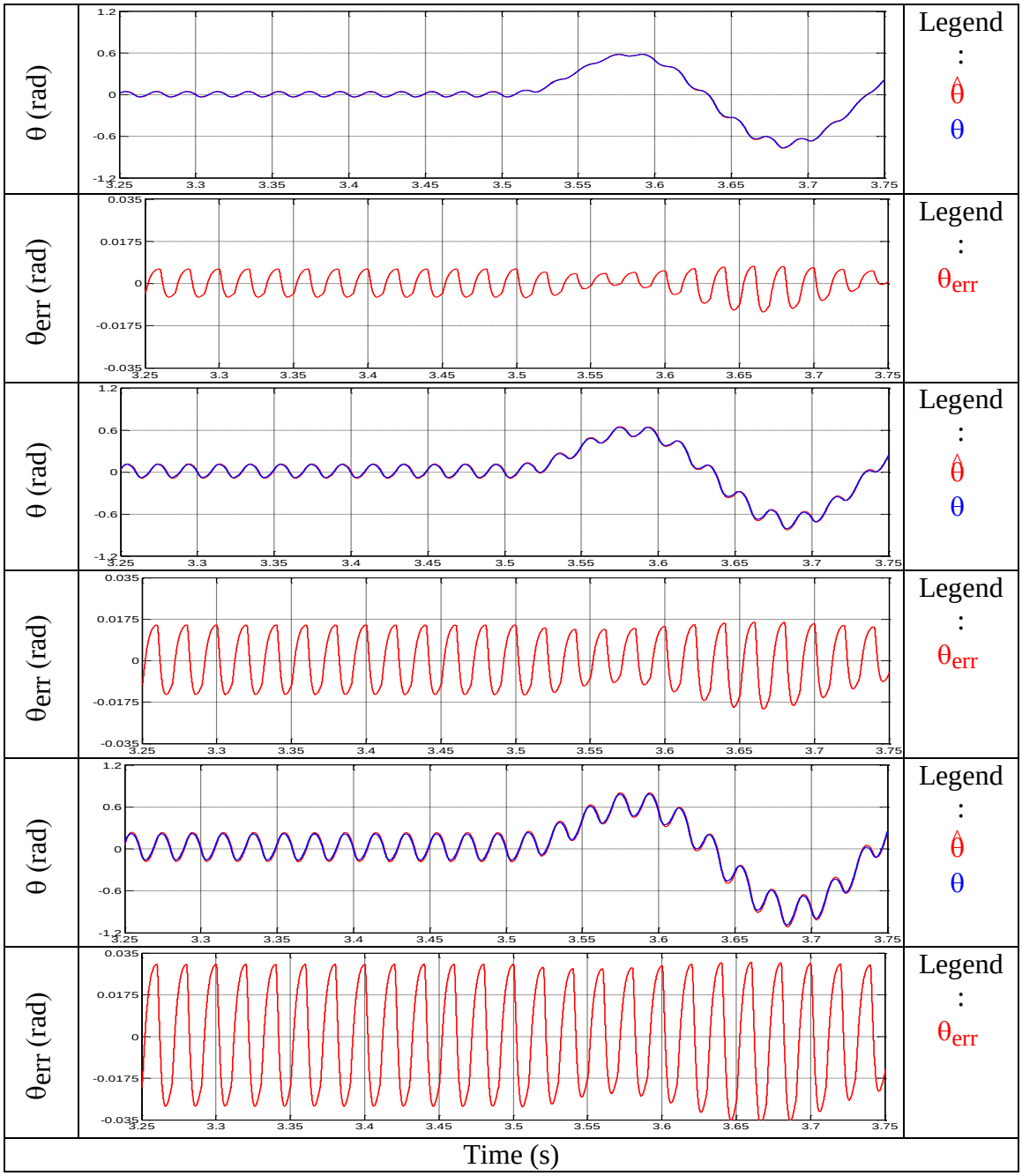

Fig. 4.2- Position estimation and position estimation error at 50Hz pulsating frequency, at zero speed (ω_{rm} = 0rad/s) and for different load torque values (From top to bottom: T_L= 0.2N-m (0.04pu), T_L= 0.5N-m (0.1pu), T_L= 1N-m (0.2pu))

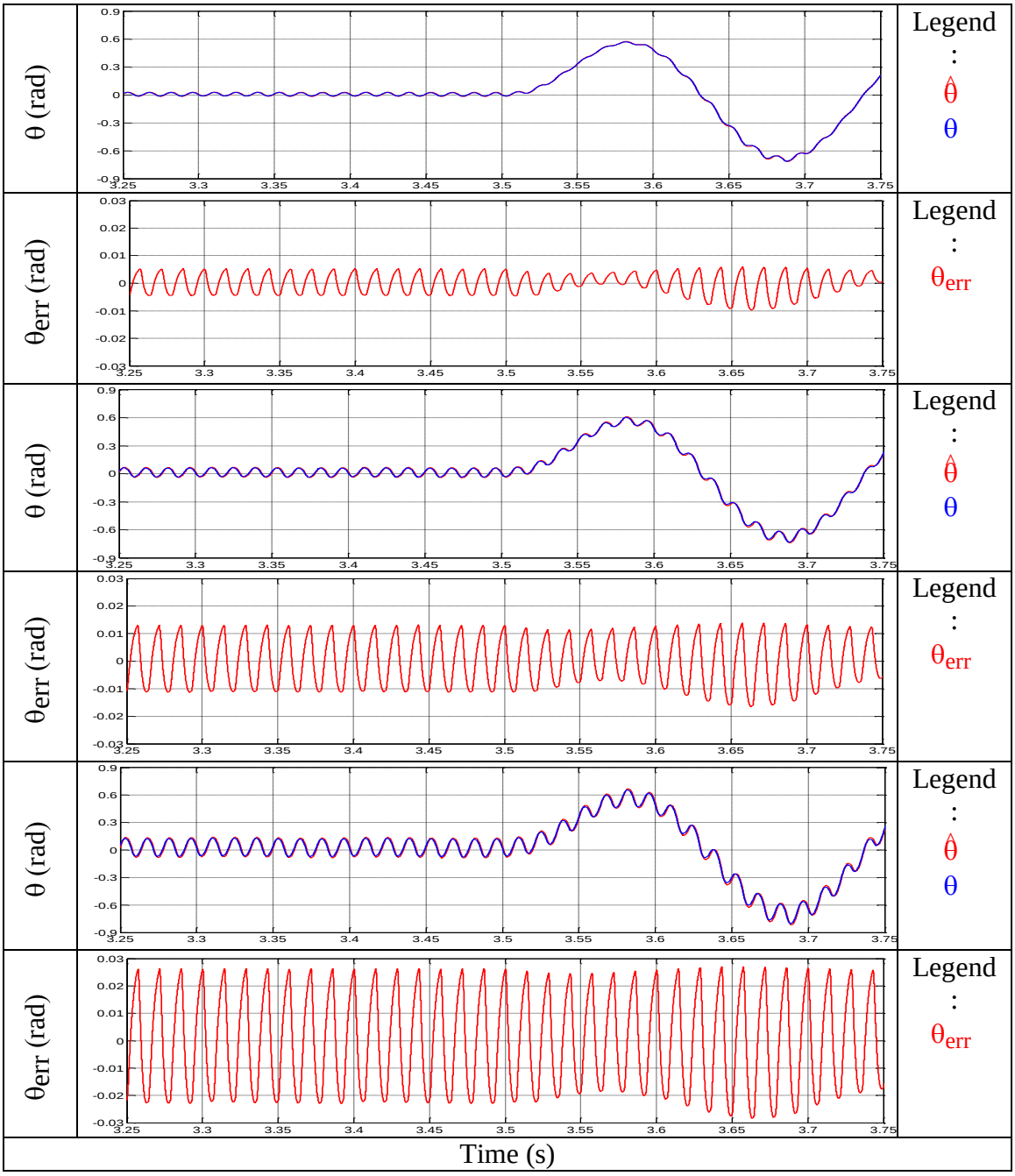

Fig. 4.3- Position estimation and position estimation error at 70Hz pulsating frequency, at zero speed (ω_{rm} = 0rad/s) and for different load torque values (From top to bottom: T_L= 0.2N-m (0.04pu), T_L= 0.5N-m (0.1pu), T_L= 1N-m (0.2pu))

4.1.2 Position estimation at 10rad/s

This subsection shows the position estimation when running the machine at 10rad/s mechanical (Fig. 4.5-Fig. 4.7).

From the simulation results shown in this section, it may be concluded that a similar performance has been obtained compared to the latter case at standstill. The biggest position error is 0.035 electrical radians which is equivalent to 2 electrical degrees.

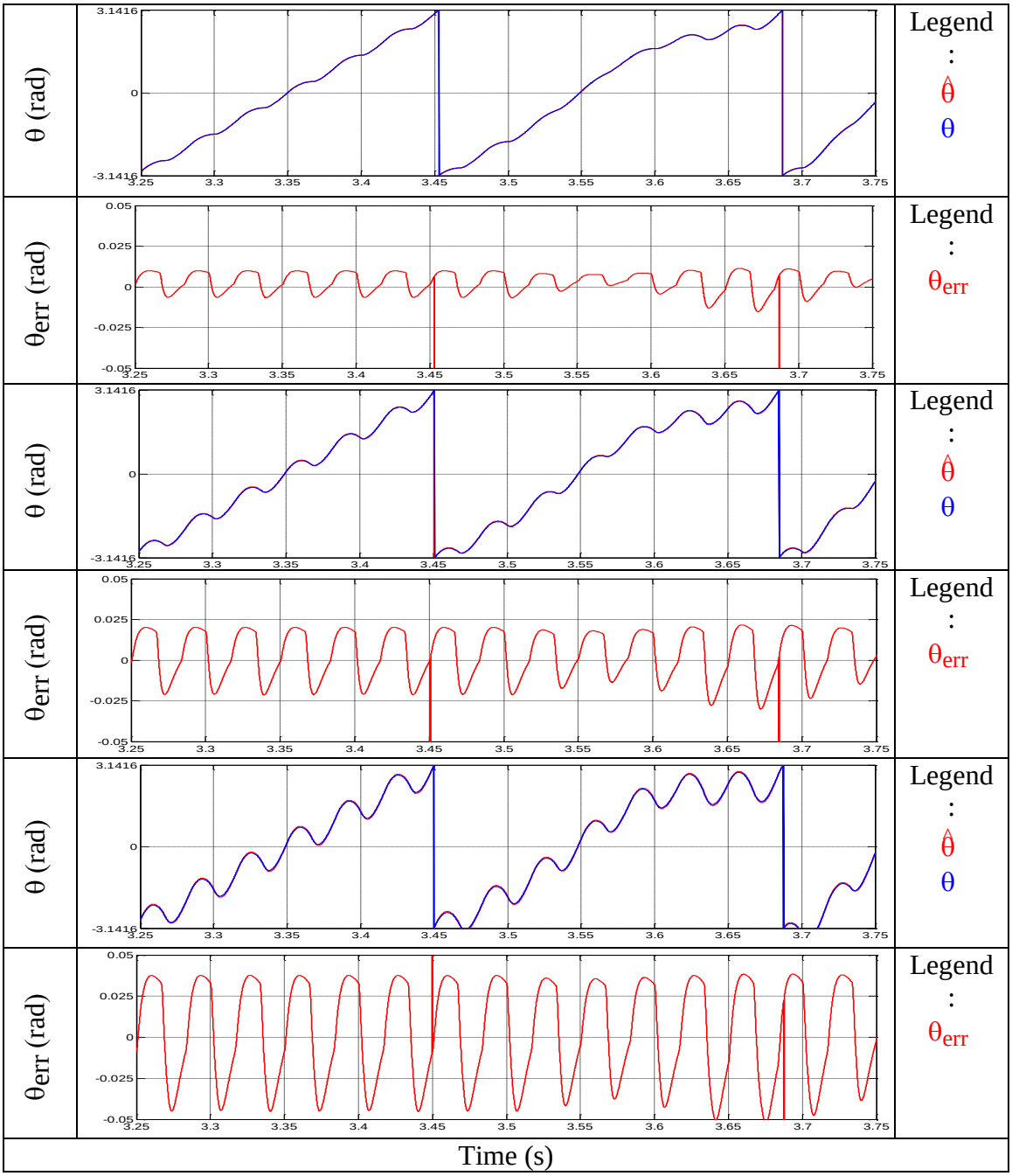

Fig. 4.5- Position estimation and position estimation error at 30Hz pulsating frequency, at 10rad/s (ω_{rm} = 10rad/s) and for different load torque values (From top to bottom: T_L= 0.2N-m (0.04pu), T_L= 0.5N-m (0.1pu), T_L= 1N-m (0.2pu))

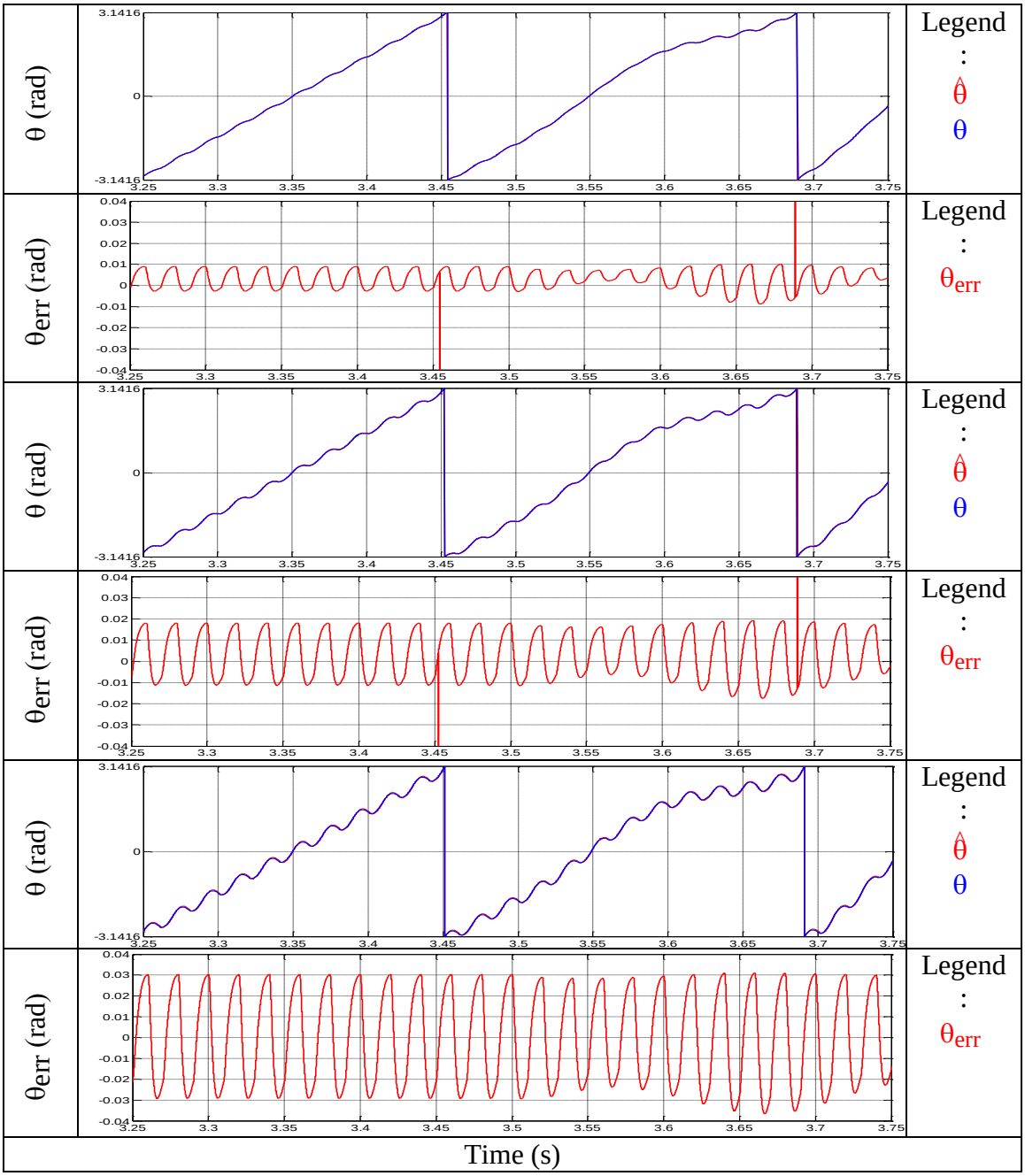

Fig. 4.6- Position estimation and position estimation error at 50Hz pulsating frequency, at 10rad/s (ω_{rm} = 10rad/s) and for different load torque values (From top to bottom: T_L= 0.2N-m (0.04pu), T_L= 0.5N-m (0.1pu), T_L= 1N-m (0.2pu))

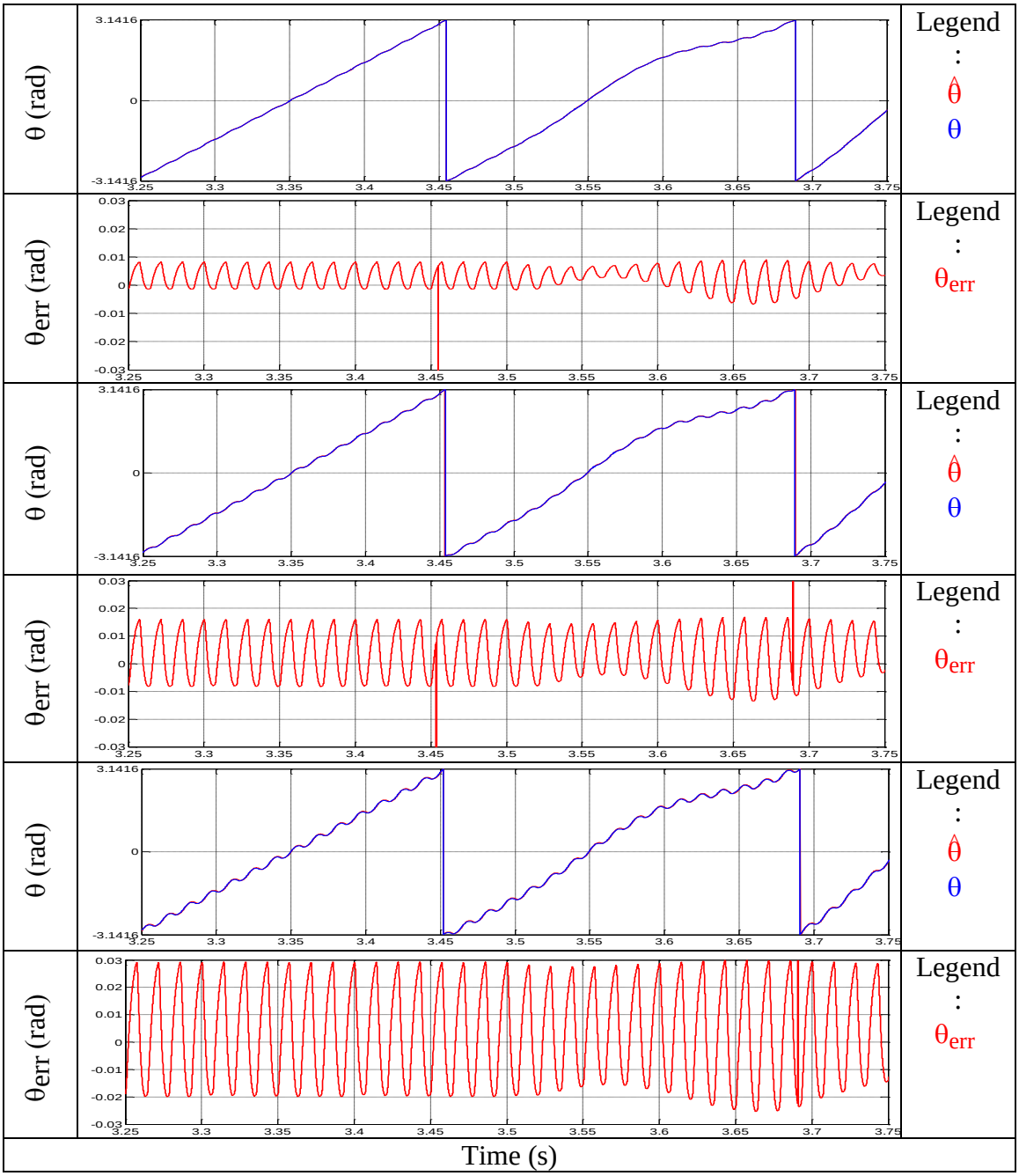

Fig. 4.7- Position estimation and position estimation error at 70Hz pulsating frequency, at 10rad/s (ω_{rm} = 10rad/s) and for different load torque values (From top to bottom: T_L= 0.2N-m (0.04pu), T_L= 0.5N-m (0.1pu), T_L= 1N-m (0.2pu)

4.1.3 Velocity estimation at zero speed

The same tests that have been run to obtain the position estimation simulation results previously have been repeated to present the simulation results concerning speed estimation (Fig. 4.8-Fig. 4.10). In this regard, the simulation results show a bigger error in the estimation compared to the position ones.

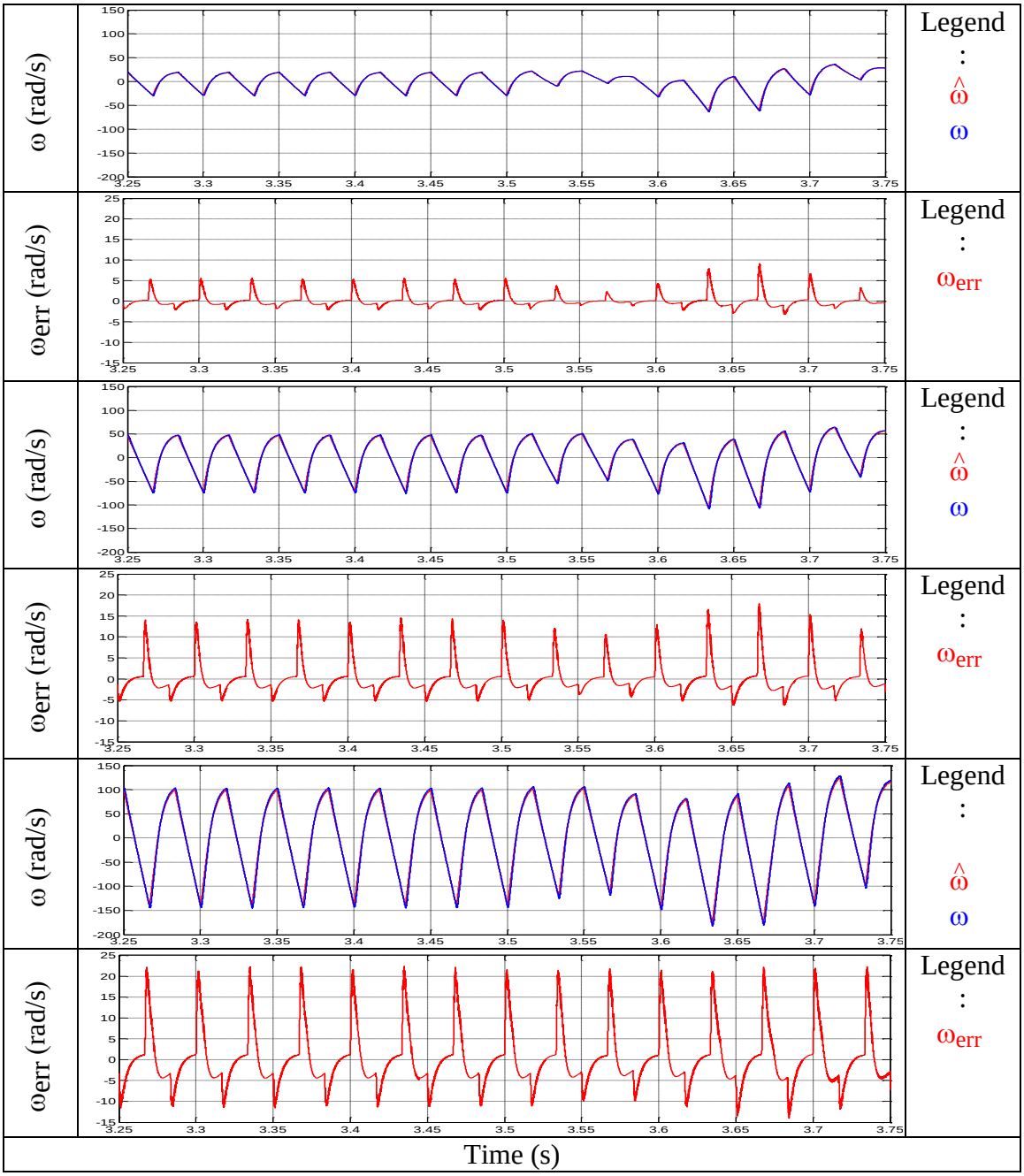

Fig. 4.8- Velocity estimation and velocity estimation error at 30Hz pulsating frequency, at zero speed (ω_{rm} = 0rad/s) and for different load torque values (From top to bottom: T_L= 0.2N-m (0.04pu), T_L= 0.5N-m (0.1pu), T_L= 1N-m (0.2pu))

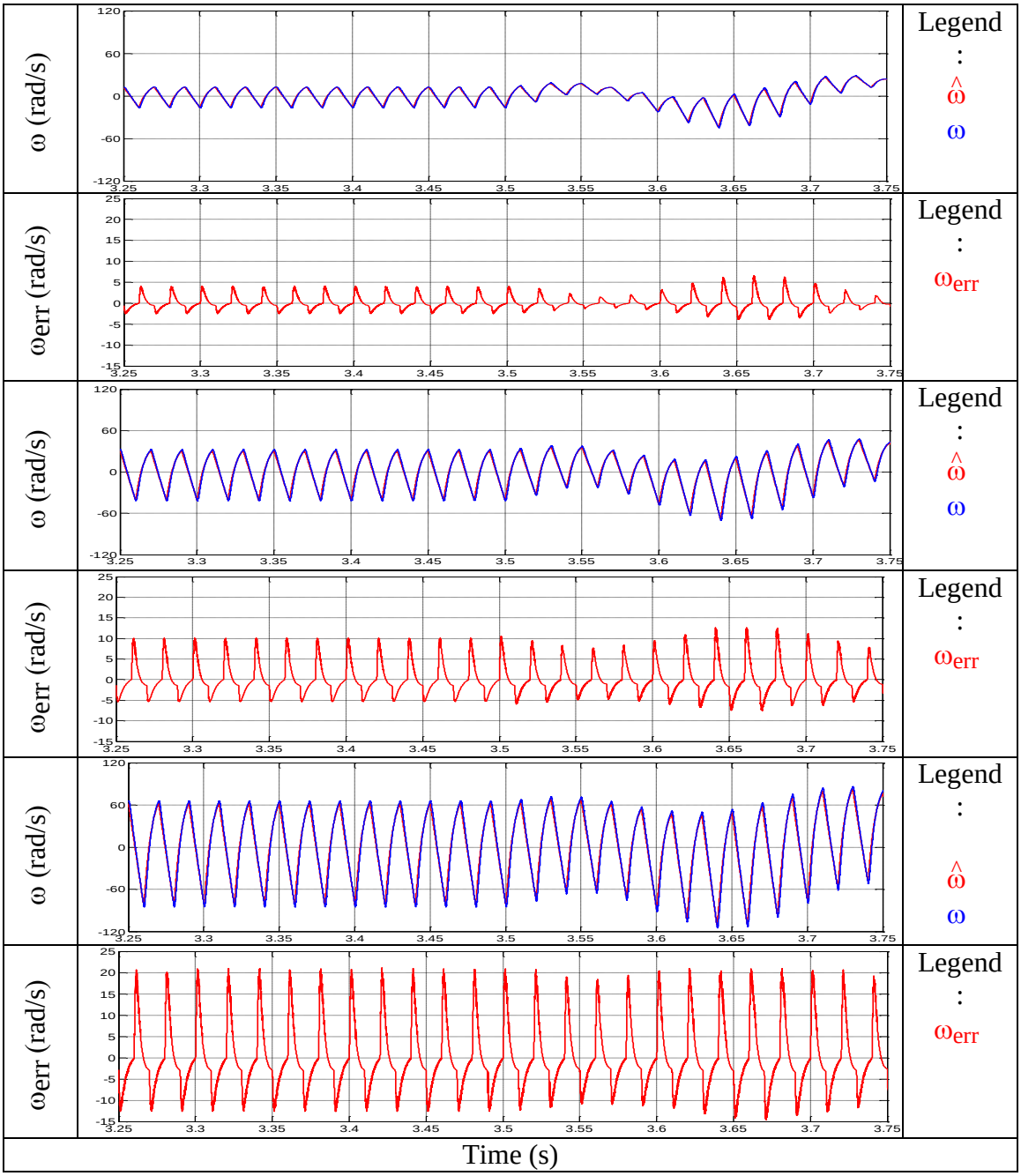

Fig. 4.9- Velocity estimation and velocity estimation error at 50Hz pulsating frequency, at zero speed (ω_{rm} = 0rad/s) and for different load torque values (From top to bottom: T_L= 0.2N-m (0.04pu), T_L= 0.5N-m (0.1pu), T_L= 1N-m (0.2pu))

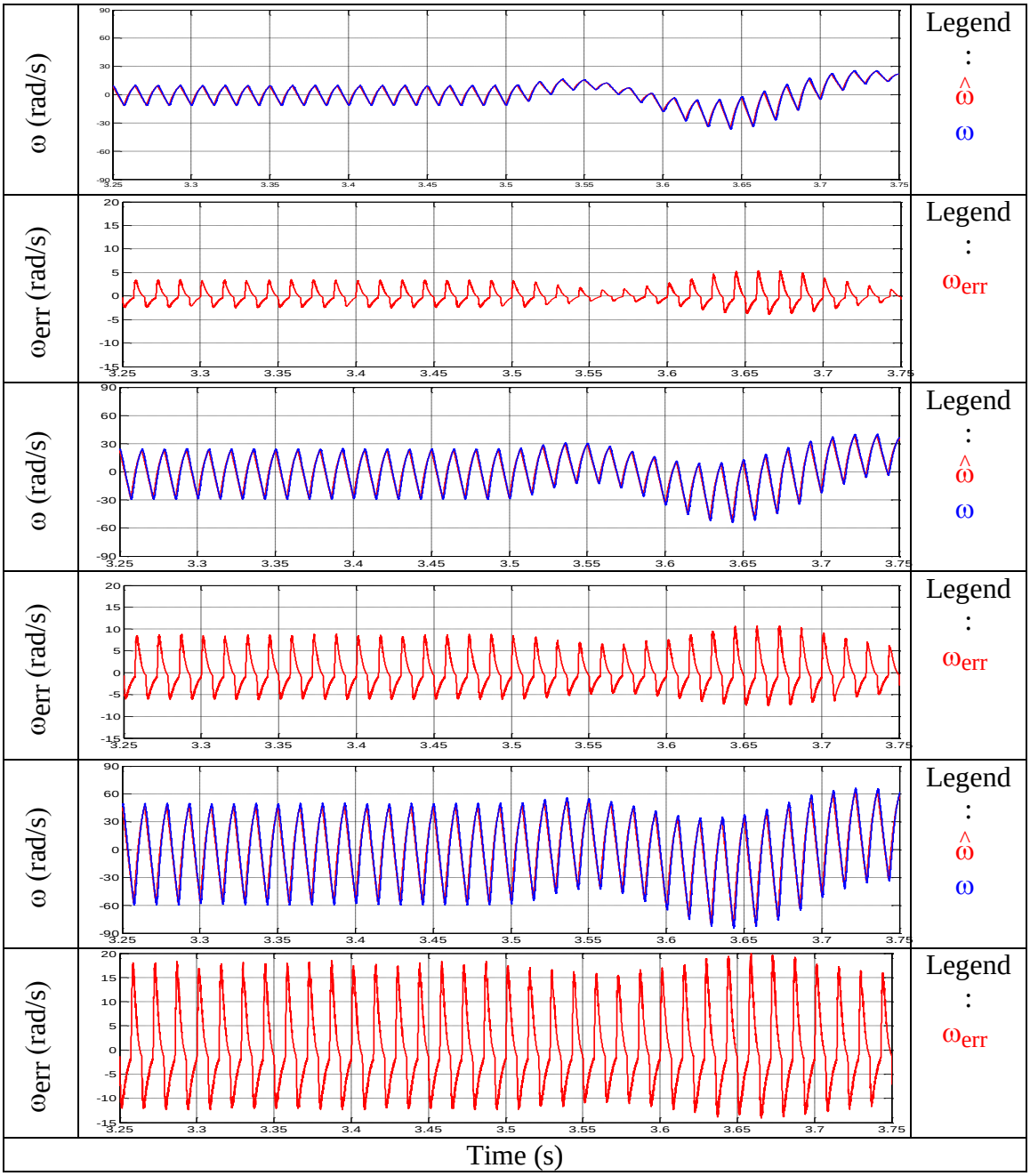

Fig. 4.10- Velocity estimation and velocity estimation error at 70Hz pulsating frequency, at zero speed (ω_{rm} = 0rad/s) and for different load torque values (From top to bottom: T_L= 0.2N-m (0.04pu), T_L= 0.5N-m (0.1pu), T_L= 1N-m (0.2pu))

4.1.4 Velocity estimation at 10 rad/s

Lastly, the speed estimation results are obtained (Fig. 4.11-Fig. 4.14) and presented in this sub section for a given mechanical speed of 10rad/s.

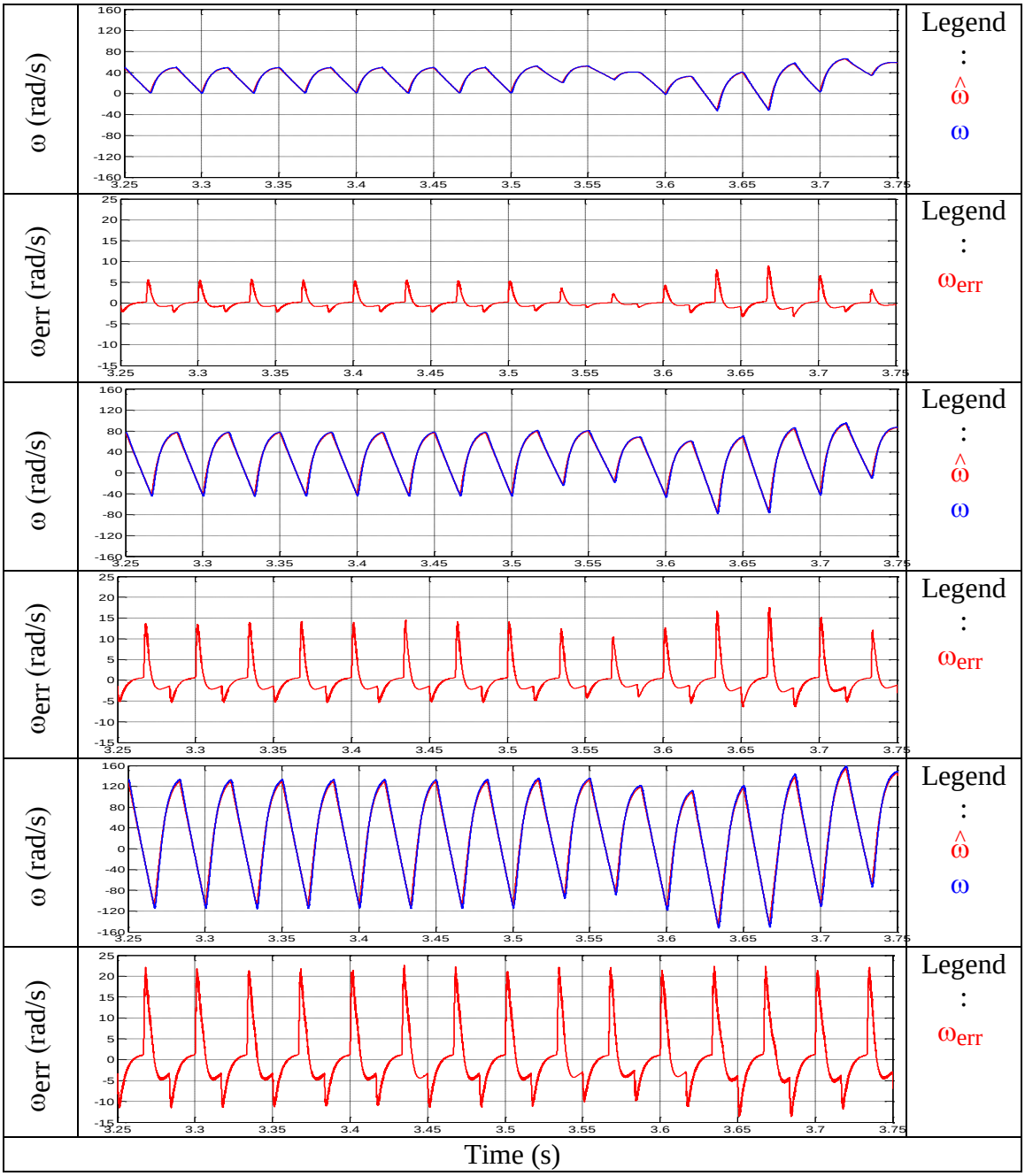

Fig. 4.11- Velocity estimation and velocity estimation error at 30Hz pulsating frequency, at ω_{rm} = 10rad/s and for different load torque values (From top to bottom: T_L= 0.2N-m (0.04pu), T_L= 0.5N-m (0.1pu), T_L= 1N-m (0.2pu))

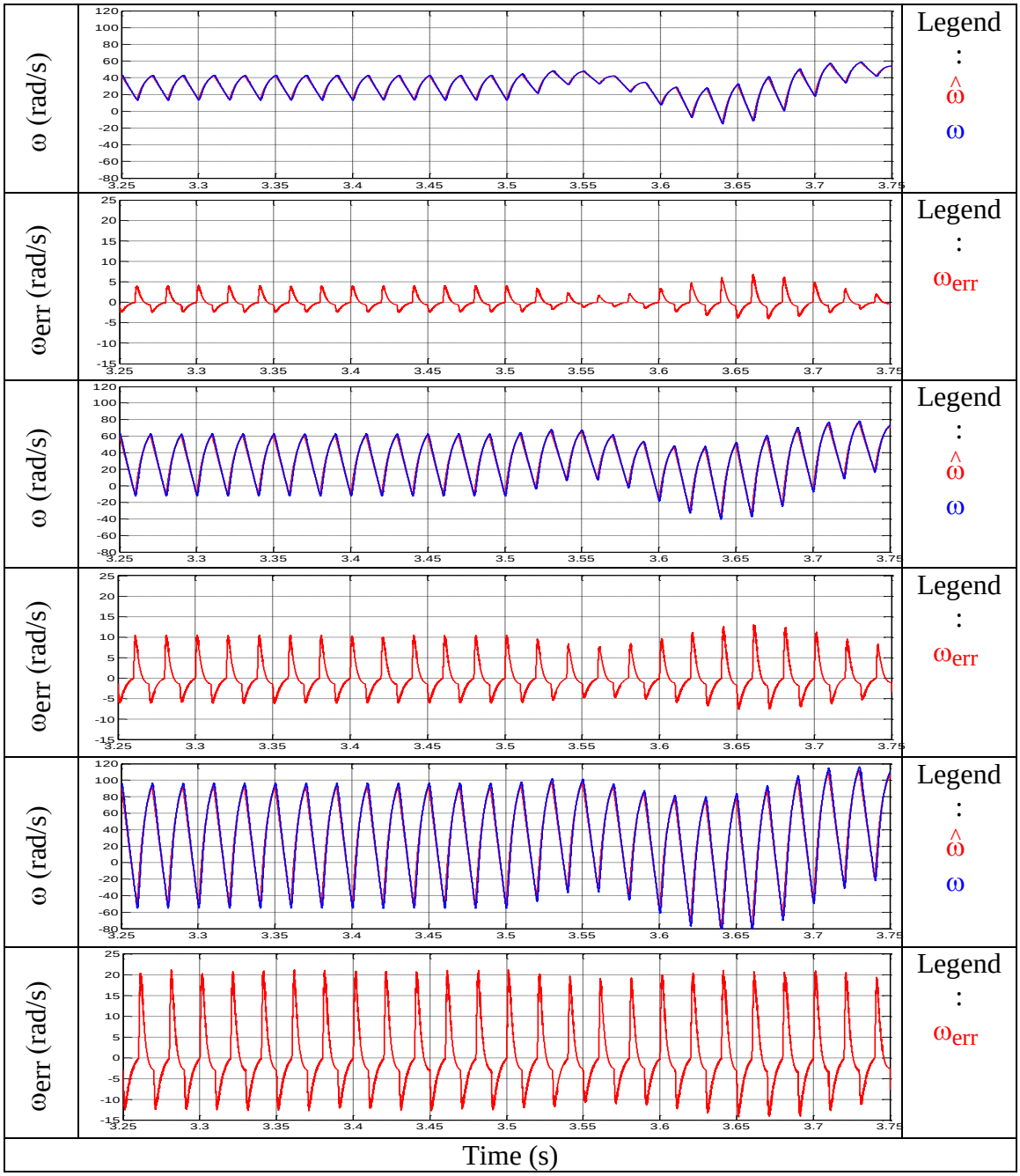

Fig. 4.12- Velocity estimation and velocity estimation error at 50Hz pulsating frequency, at ω_{rm} = 10rad/s and for different load torque values (From top to bottom: T_L= 0.2N-m (0.04pu), T_L= 0.5N-m (0.1pu), T_L= 1N-m (0.2pu))

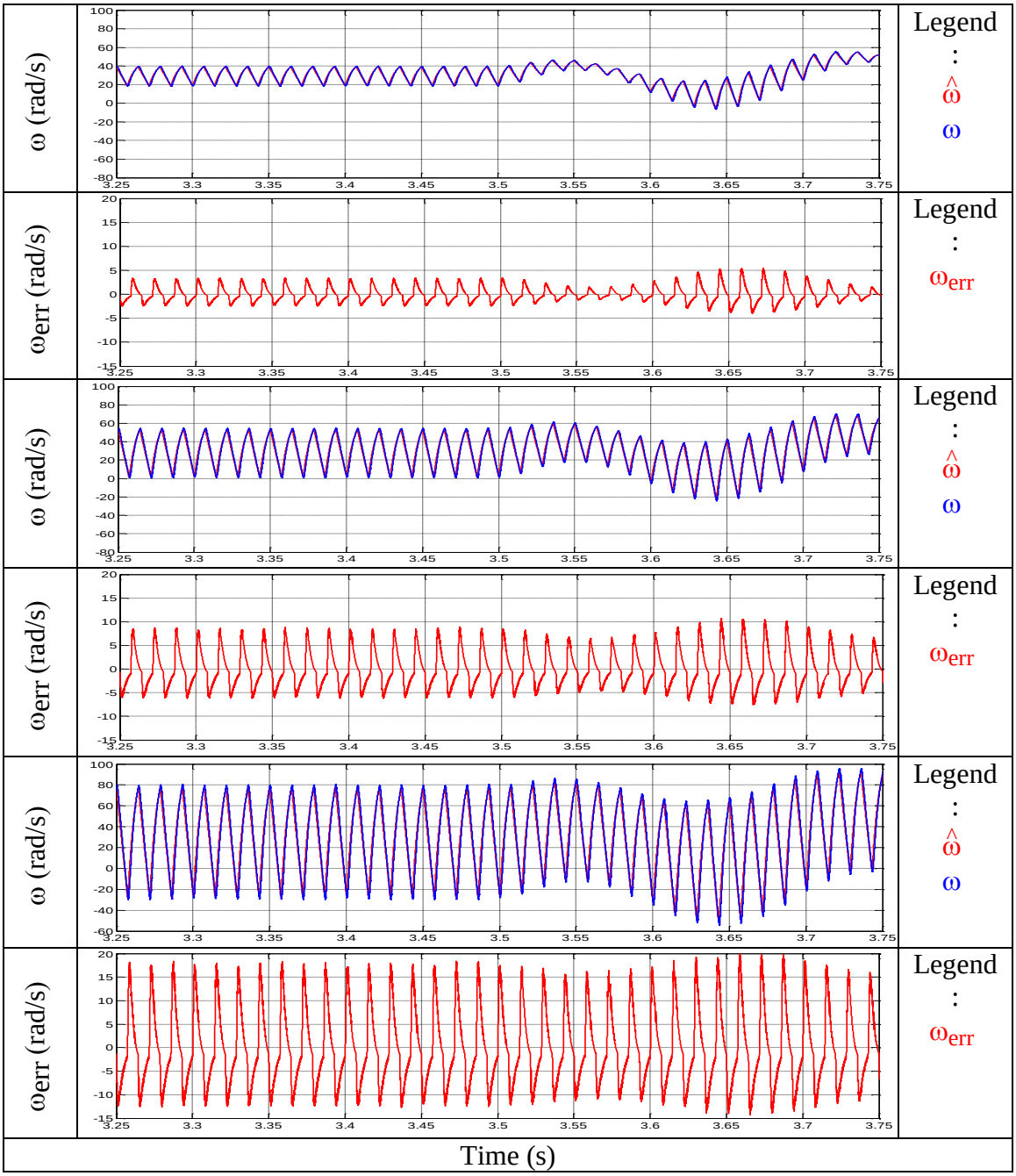

Fig. 4.13- Velocity estimation and velocity estimation error at 70Hz pulsating frequency, at ω_{rm} = 10rad/s and for different load torque values ((From top to bottom: T_L= 0.2N-m (0.04pu), T_L= 0.5N-m (0.1pu), T_L= 1N-m (0.2pu))

4.2 Currents values

The RMS value of the currents in the motor is the main drawback of pulsing the current on and off with a 50% duty cycle. In Fig. 4.14 the currents measurements are shown in the synchronous reference frame, when using a pulsating frequency (f_p) of 50Hz and different load torque values (T_L= 0.2N-m (0.04pu), T_L= 0.5N-m (0.1pu), T_L= 1N-m (0.2pu)). In this simulation a sinusoidal torque disturbance (0.1N-m and 5Hz) is also introduced at 3.5s. As it can be in Fig. 4.14 the pulsating current value increases and it can get up to 9A in the last case (T_L=1N-m). Due to this fact, using a 50% duty cycle is not very appropriate.

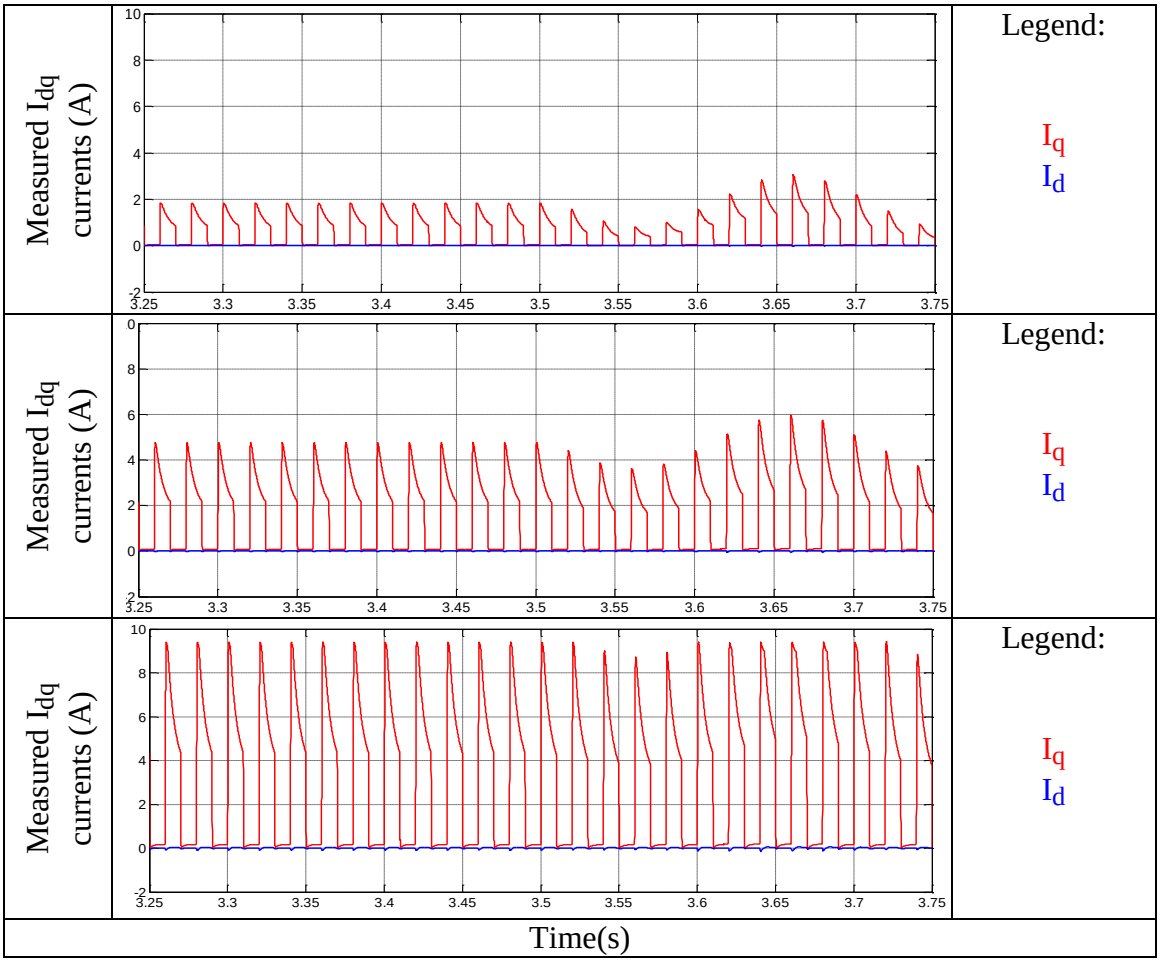

Fig. 4.14- Measured dq currents in the synchronous reference frame at 50Hz pulsating frequency, at ω_{rm} = 0rad/s and for different load torque values ((From top to bottom: T_L= 0.2N-m (0.04pu), T_L= 0.5N-m (0.1pu), T_L= 1N-m (0.2pu))

4.3 Dynamic stiffness of the Simulation Model

The dynamic stiffness shows the disturbance rejection capabilities of the system. It can be calculated by using the position or the speed estimates. In either case, in the y-axis the

disturbance torque over the position or speed ratio is shown $\left(\left|\frac{T_d}{\omega}\right| \left|\frac{T_d}{\theta}\right|\right)$. A larger dynamic stiffness means a better system behavior against torque perturbations.

In order to measure the dynamic stiffness, a chirp signal of 0.2N-m magnitude (0.04pu) from that varies from 0.01Hz to 1000Hz within 75 seconds is introduced as a load disturbance, being the dc load 0N-m.

4.3.1 Dynamic Stiffness for different Motion Controller Bandwidths

The following figure (Fig. 4.15) shows the comparison of the dynamic stiffness (DS) of the simulation model for different motion controller bandwidths (10, 20, 30 Hz), at zero speed, T_L=0, f_p=50Hz and comparing for each of them the DS using measured and estimated feedback respectively.

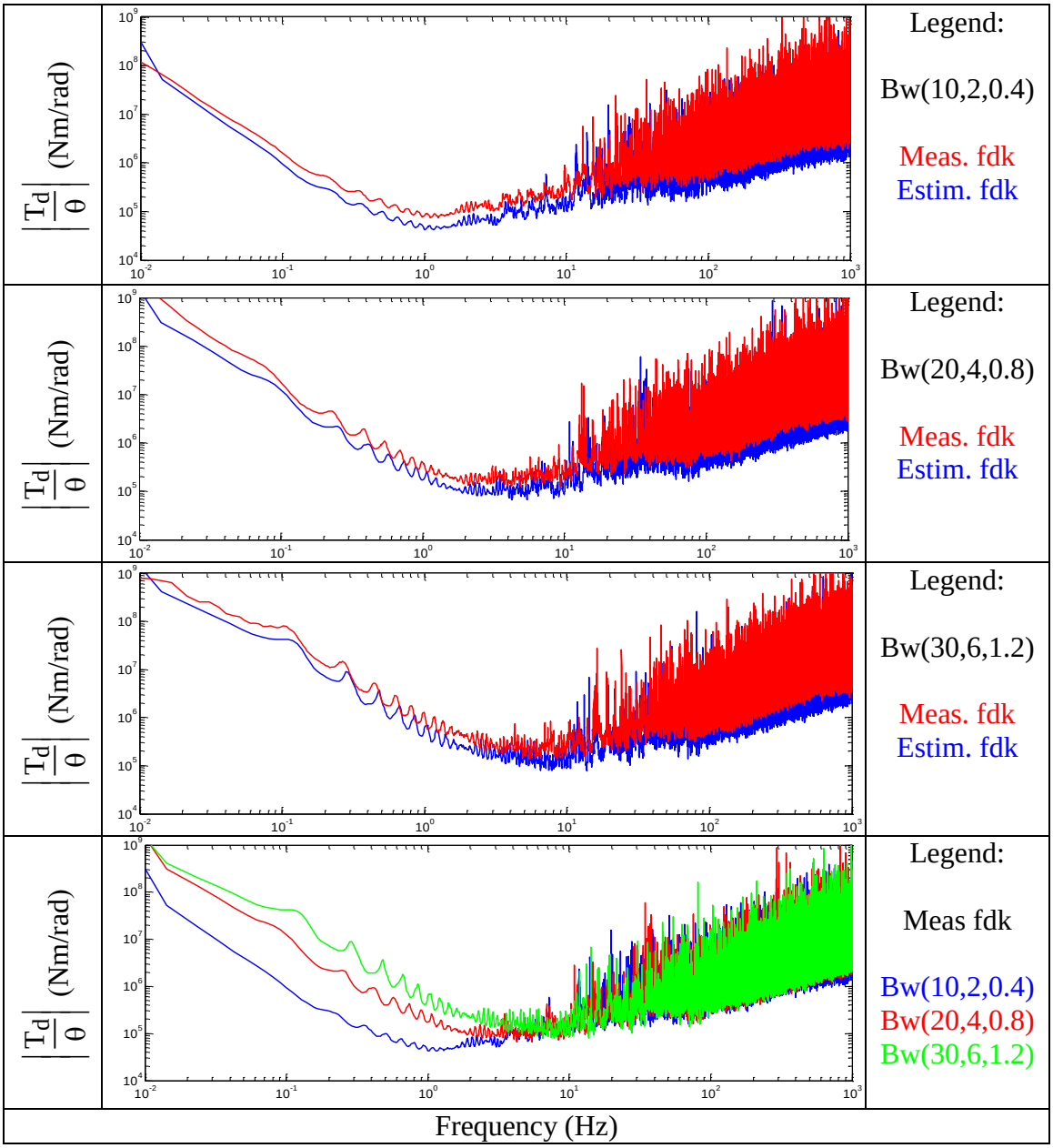

Fig. 4.15 Dynamic Stiffness at f_p=50Hz, T_L=0N-m, ω_{rm} = 0rad/s and using the aforementioned chirp signal with measured and estimated feedback for different speed controller bandwidths (From top to bottom: $bandwidth_\omega$= 10Hz, $bandwidth_\omega$= 20Hz, $bandwidth_\omega$= 30Hz, comparison of the three previous plots using estimated feedback).

As it can be seen in Fig. 4.15 the stiffness of the system is lower when using estimated feedback as it could have been predicted. Nevertheless, it does not make much of a difference, being the system quite stiff when using self-sensing.

Furthermore, when comparing the DS of the system for different motion controller bandwidths, the higher the speed controller bandwidth is, the more stiff the system is.

4.3.2 Dynamic Stiffness for different pulsing frequencies.

Fig. 4.16 shows different DS curves for different pulsing frequencies (30, 60, 90Hz) and at zero mean speed. It can be seen that the system is slightly stiffer specially at low frequencies for higher pulsing frequencies.

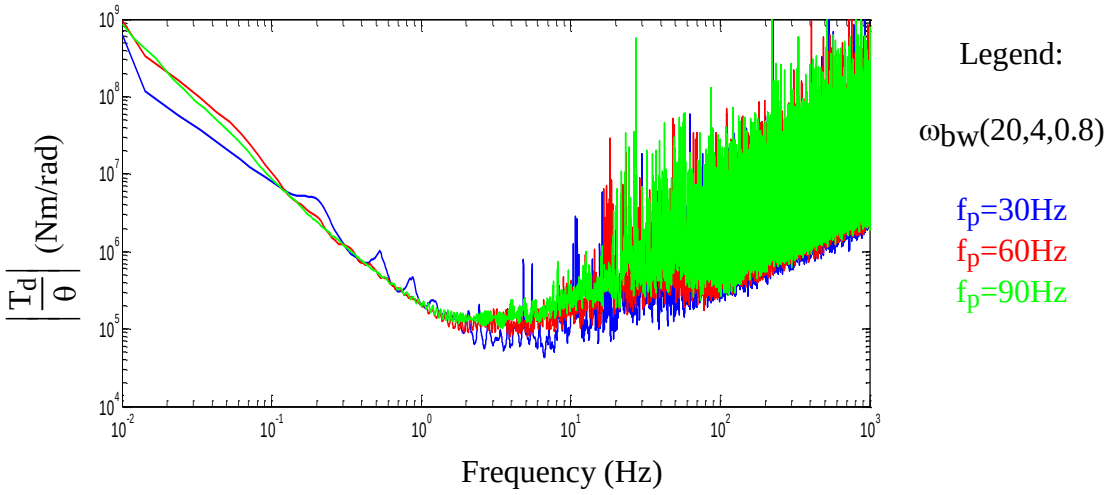

Fig. 4.16- Dynamic Stiffness with a 20Hz motion controller and for different pulsing frequencies, T_L=0N-m, ω_{rm} = 0rad/s and using the same chirp signal as in the latter case.

From top to bottom: f_p= 30Hz, f_p= 60Hz f_p= 90Hz.

4.4 Parameter sensitivity

The parameter sensitivity analysis shows how well the self-sensing works when misestimating the electrical parameters (L_s and R_s). In order to carry out this analysis the estimated L_s and R_s values are changed by adding a 10, 20 and 30% of its real value and the position and speed estimates are shown in Fig. 4.17.

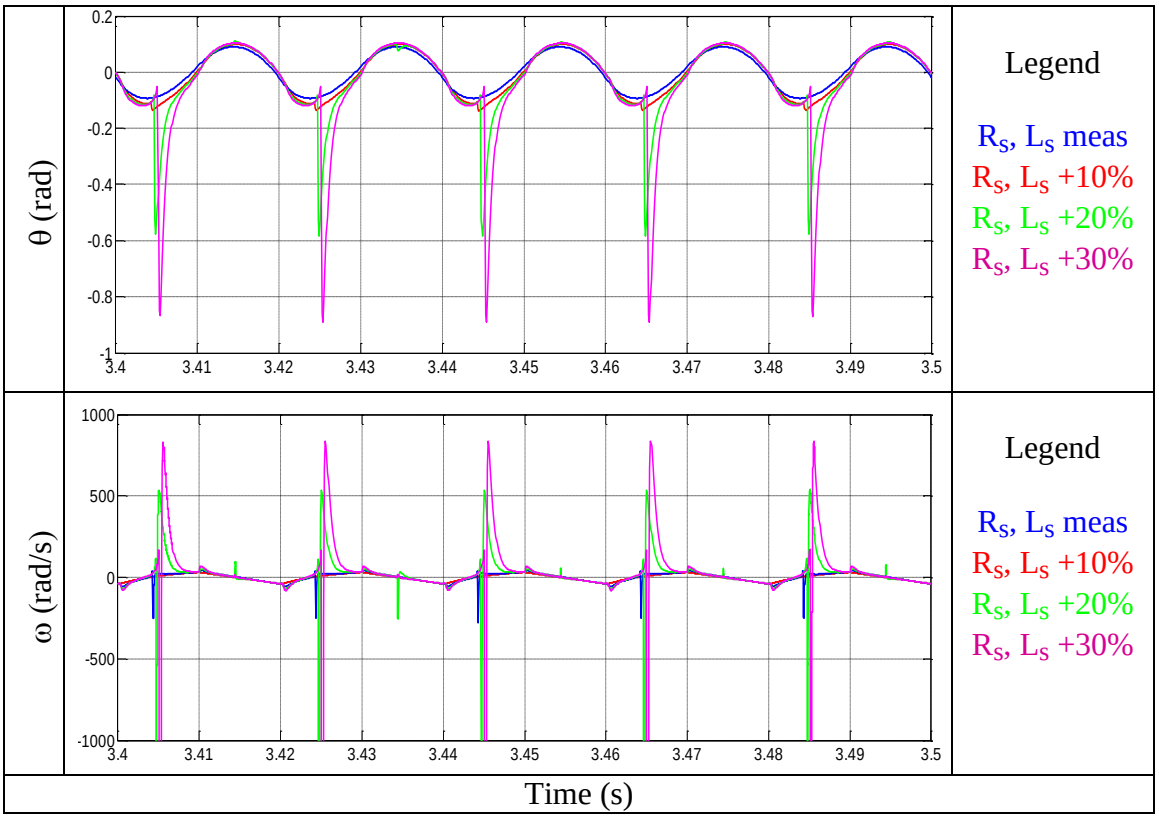

Fig. 4.17- Parameter Sensitivity Analysis, when R_s and L_s values are off my 10, 20 and 30% respectively. T_L=0.5N-m, f_p=50Hz, ω_{rm} = 0rad/s .

Both the position and speed estimates closely track the real values even when the Motor parameters (R_s and L_s) are misestimated by a 30%. Nevertheless, there is a

transient error that may have been mitigated by using an observer for position estimation rather than a PLL.

4.5 Summary

This chapter has shown the simulation results regarding both position and velocity estimation at standstill and at 10rad/s mechanical. Different pulsing frequencies for the controller current have been tried, as well as different load torque values. The results prove that the methodology produces accurate estimates.

The current values of the motor due to the 50% duty cycle pulsating torque have been proved to be too high for the SPMSM that is being used. This methodology has some room of improvement by reducing the amount of time the torque is pulsed off and therefore its peak-to-peak value.

Furthermore, the DS of the simulation model has been analyzed, for different motion controller bandwidths and also varying the pulsing frequency. This analysis has shown a better stiffness performance at low speeds for higher motion controller bandwidths as well as for higher pulsing frequencies. At high frequencies the stiffness is approximately the same.

Lastly, a parameter sensitivity analysis has been carried out, showing that the system is capable of tracking position and velocity even when the parameters L_S and R_S are misestimating by a 30% of their actual value.

Chapter 5

Conclusions and Future Work

This chapter provides a set of conclusions about the research that has been carried out in this thesis. It also gives directions concerning future work on this research field.

5.1 Conclusions

The first conclusion from the interpretation of the patent is that this methodology cannot work without torque load as it is needed for the machine to produce a pulsating torque and therefore generate back-EMF at zero speed.

The second conclusion of this research is that when using a 50% duty cycle to pulsate the commanded torque signal, twice the peak-to-peak value of the AC torque command is twice the amplitude value of the DC torque command.

Regarding the frequencies the controller is being pulsed at, it has been shown through simulation that they must be increased accordingly with the load torque increase to achieve having a more accurate position and velocity estimates.

As for the induced back-EMF, it has been shown that by pulsing the current the induced back-EMF is large enough to allow a good tracking of it, being the magnitude within a range of 1-6V when the pulsing frequency varies from 100-25Hz respectively.

This thesis also includes evaluation of the simulation model via the dynamic stiffness analysis and parameter sensitivity analysis for a better understanding of the limitations and validity of the model.

Veltman flux tracking methodology at zero-to-low speeds claims to pulse the controller current on and off at low frequencies but he does not specify in which range. In this thesis frequencies below 100Hz were considered, obtaining better estimation results with higher frequencies for higher load torque values.

The benefit of this methodoly is that it is intended to work for any electric machine, as the back-EMF can be induced in any kind of electrical machine that produces torque.

5.2 Contributions

The contributions of this thesis are the development and documentation of a simulation model that allows simulating the methodology patented by Veltman in his patent [27] for the zero-to-low speeds range on an SPMSM and that achieves the results that Veltman claimed in his invention.

5.3 Future Work

For future work, this methodology should be evaluated by reducing the duty cycle so the torque is pulsed off for less time, allowing this having a much less AC current values in the motor and less severe pulsation.

Also, signal injection would be another solution to consider generating a pulsating current in the motor that allows a sufficient back-EMF generation rather than pulsating the torque.

Regarding the limitation of zero torque load, an AC torque signal could be introduced in the motor to generate some pulsating torque at zero speeds.

Analyze the dynamic stiffness under different load torque conditions and speeds should be an interesting test to do in the future work as well as investigating the limitations of using very low and very high pulsing frequencies.

Lastly, an experimental evaluation of this methodology should be done on a test bench and tested on a real SPMSM to know more about the practical limitations of this approach. Also, once the limitations of flux tracking self-sensing are known, it would be interesting to implement some other self-sensing strategies for zero-to-low speeds position and velocity estimation such as high frequency injections methods or saliency tracking methods.

Chapter 6

External Master Thesis

Bibliography

[1] Xiaocan Wang, Wei Xie; Ralph Kennel and Dieter Gerling, "Sensorless Control of a Novel IPMSM Based on High-Frequency Injection," Institute for Electrical Drive Systems and Power Electronics, Technical University of Munich, Electrical Drives and Actuators, University of Federal Defense Munich, EPE'13 ECCE Europe, ISBN: 978-90-75815-17-7 and 978-1-4799-0114-2

[2] Hyunbae Kim, "On-Line Parameter Estimation, Current Regulation, and Self-Sensing for IPM Synchronous Machine Drives," Doctor of Philosophy Thesis, Mechanical Engineering, University of Wisconsin-Madison, 2004

[3] Shih-Chin Yang, "Position Sensing of Surface Permanent Magnet Machine Using High Frequency Signal Injection," Doctor of Philosophy Thesis, Mechanical Engineering, University of Wisconsin-Madison, 2011

[4] Robert W. Hejny, "Degradation of Dynamic Stiffness at Low Speeds When Using Back-EMF Tracking for Closed Loop Speed Control," Master of Science Thesis, Mechanical Engineering, University of Wisconsin-Madison, 2008

[5] D. W. Novotny and T. A. Lipo, "Vector Control and Dynamics of AC Drives," *Oxford University Press Inc. , New York,* 1996

[6] Sungmin Kim, and Seung-Ki Sul, "Sensorless Control of AC Motor-Where are we now?," Seoul national university Power Electronics Center (SPEC), Seoul National University

[7] Shanshan Wu , David Diaz Reigosa, Yuichi Shibukawa, Michael A. Leetmaa, Robert. D. Lorenz, Yongdong Li, "Interior Permanent Magnet Synchronous Motor Design for Improving Self-sensing Performance at Very Low Speed," Dept. of Electrical Engineering, Tsinghua University, Beijing, 100084, China, Dept. of Electrical Engineering, University of Oviedo, Gijón, 33204, Spain, Nissan Motor Co., Ltd., Atsugi-shi, 243-0123, Japan, Dept. of ME & Dept. of ECE, University of Wisconsin-Madison, Madison, 53706, USA

[8] T. F. Graf, "Flux Tracking Self-Sensing and Using a Voltage Sensor for Enhanced Sensing Capabilities on SPMSM Drives," Presentation: *WEMPEC CAST Seminar*, April 2014.

[9] Fernando Briz, Michael W. Degner, Juan M. Guerrero, Antonio Zamarrón, Robert D. Lorenz,"Implementation Issues Affecting the Performance of Carrier Signal Injection Based Sensorless Controlled AC Drives," *IEEE*, pp. 2645-2652, 2001.

[10] David Díaz Reigosa, Fernando Briz, Michael W. Degner, Pablo García and Juan Manuel Guerrero, "Temperature Issues in Saliency-Tracking-Based Sensorless Methods for PM Synchronous Machines," *IEEE Transactions on Industry Applications*, vol. 47, no 3, pp. 1352-1360, May/June 2011.

[11] Robert W. Hejny and Robert D. Lorenz, "Evaluating the Practical Low Speed Limits for Back-EMF Tracking-Based Sensorless Speed Control Using Drive Stiffness as a Key Metric,", *IEEE*, 2009, 978-1-4244-2893-9

[12] J.-S. Kim and S.-K. Sul, "New approach for high-performance PMSM drives without rotational position sensors," *Power Electronics, IEEE Transactions on,* vol. 12, pp. 904-911, 1997.

[13] S. Ichikawa, M. Tomita, S. Doki, and S. Okuma, "Sensorless control of permanent-magnet synchronous motors using online parameter identification based on system identification theory," *Industrial Electronics, IEEE Transactions on,* vol. 53, pp. 363-372, 2006.

[14] Z. Peroutka, "Development of Sensorless PMSM Drives: Application of Extended Kalman Filter," *IEEE ISIE 2005*, June 2005.

[15] A. Qiu, B. Wu and H. Kojori, "Sensorless control of permanent-magnet synchronous motors using extended Kalman filter," *Canadian Conference on Electrical and Computer Engineering,* 2004, vol. 3, pp. 1557-1562, May 2004.

[16] Silverio Bolognani, Roberto Oboe, and Mauro Zigliotto, "Sensorless Full-Digital PMSM Drive With EKF Estimation of Speed and Rotor Position," *Industrial Electronics, IEEE Transactions on,* 2004, vol. 46, pp. 184-191, February 1999.

[17] M.C. Huang, A.J. Moses and F. Anayi, "The comparison of Sensorless Estimation Techniques for PMSM between Extended Kalman Filter and Flux-linkage Observer," *Industrial Electronics, IEEE Transactions on,* 2006, pp. 654-659.

[18] Borsje, P., Chan, T.F., Wong, Y.K. and Ho, S.L., "A Comparative Study of Kalman Filtering for Sensorless Control of a Permanent-Magnet Synchronous Motor Drive," *Industrial Electronics, IEEE Transactions on,* 2005, pp. 815-822.

[19] Silverio Bolognani, Luca Tubiana, and Mauro Zigliotto, "Extended Kalman Filter Tuning in Sensorless PMSM Drives," *Industrial Electronics, IEEE Transactions on,* 2003, vol. 39, pp. 1741-1747, November/December 2003.

[20] Zdeněk Peroutka, Václav Šmídl and David Vošmik, "Challenges and Limits of Extended Kalman Filter based Sensorless Control of Permanent Magnet Synchronous Machine Drives," *University of West Bohemia, Pilsen, Institute of Information Theory and Automation.*

[21] Zedong Zheng, Yongdong Li, Maurice Fadel, "Sensorless Control of PMSM Based on Extended Kalman Filter," *Lab. LAPLACE UMR-CNRS 5213, INP-ENSEEIHT, Department of Electrical Engineering, Tsinghua University*.

[22] H. Kim, M. C. Harke and R. D. Lorenz, "Sensorless Control of Interior Permanent-Magnet Machine Drives with Zero-Phase Lag Position Estimation," *IEEE Transactions on Industry Applications*, vol. 39, no. 6, pp. 1726–1733, November 2003.

[23] M.W. Degner, R.D. Lorenz, "Using Multiple Saliencies for the Estimation of Flux, Position, and Velocity in AC Machines," *IEEE Industry Applications Society*, Annual Meeting, New Orleans, Louisiana, October 1997.

[24] Gaolin Wang, Hanlin Zhan, Guoqiang Zhang, Xianguo Gui and Dianguo Xu, "Adaptive Compensation Method of Position Estimation Harmonic Error for EMF-Based Observer in Sensorless IPMSM Drives," *IEEE Transactions on Power Electronic*, vol. 29, no 6, pp. 3055-3064, June 2014.

[25] Eisenhawer de M. Fernandes, Alexandre C. Oliveira, Antonio M. N. Lima, Cursino B. Jacobina and Welflen R. N. Santos, "Self-sensing Control of PMSM Motor for Wide-speed Range Operation," *Industrial Electronics, IEEE Transactions on, 2013, pp. 814-820.*

[26] Gaolin Wang, Rongfeng Yang, and Dianguo Xu, "DSP-Based Control of Sensorless IPMSM Drives for Wide-Speed-Range Operation," *IEEE Transactions on Industrial Electronics*, vol. 60, no 2, pp. 720-727, February 2013.

[27] Andre Veltman, "Method and a Device for Sensorless Estimating the Relative Angular Position Between the Stator and the Rotor of a Three-Phase Synchronous Motor," *United States Patent*, Patent no US 6,552,509 B2, April 2003

[28] Michael W. Degner, "Flux, Position, and Velocity Estimation in AC Machines Using Carrier Signal Injection," Doctor of Philosophy Thesis, Mechanical Engineering, University of Wisconsin-Madison, 1998

[29] R. Krishnan, "Permanent Magnet Synchronous and Brushless DC Motor Drives," Electrical and Computer Engineering Department, Virginia Tech, Blacksburg, Virginia, U.S.A., CRC Press, Taylor & Francis Group, 2010, International Standard Book Number: 978-0-8247-5384-9

[30] R. S. Miranda, E. M. Fernandes, C. B. Jacobina, A. M. N. Lima, A. C. Oliveira, M. B. R. Correa, "Sensorless Control of a PMSM Synchronous Motor at Low Speed,", *Departamento de Engenharia Elétrica*, Universidade Federal de Campina Grande, 58109-970 Campina Grande - PB – Brazil

[31] Michael C. Harke, Luiz A. de S. Ribeiro, and Robert D. Lorenz, "Disturbance rejection limitations of back-EMF based sensorless PM drives,", Hamilton Sundstrand, Cefet-Ma- Brazil, Univ. of Wisconsin – Madison

[32] Eisenhawer de M. Fernandes, Alexandre C. Oliveira, Antonio M. N. Lima, Cursino B. Jacobina, and Welflen R. N. Santos, "A Comparative Evaluation of Signal Injection Methods for PMSM Self-sensing Control," *Industrial Electronics, IEEE Transactions on,* 2013, vol. 39, pp. 821-827.

[33] Luiz A. de S. Ribeiro, Michael C. Harke, Robert D. Lorenz, "Dynamic Properties of Back-EMF Based Sensorless Drives," *IEEE,* 2006, pp. 2026-2033.